KINEMATIC AND MECHANICAL RECONSTRUCTION OF WALKER RIDGE STRUCTURES, DEEPWATER GULF OF MEXICO

A Thesis

by

OLUWATOSIN ENIOLA MAJEKODUNMI

Submitted to the Office of Graduate Studies of
Texas A&M University
in partial fulfillment of the requirements for the degree of

MASTER OF SCIENCE

December 2009

Major Subject: Geology

KINEMATIC AND MECHANICAL RECONSTRUCTION OF WALKER RIDGE STRUCTURES, DEEPWATER GULF OF MEXICO

A Thesis

by

OLUWATOSIN ENIOLA MAJEKODUNMI

Submitted to the Office of Graduate Studies of
Texas A&M University
in partial fulfillment of the requirements for the degree of

MASTER OF SCIENCE

Approved by:

Chair of Committee,	David V. Wiltschko
Committee Members,	John H. Spang
	William R. Bryant
Head of Department,	Andreas K. Kronenberg

December 2009

Major Subject: Geology

ABSTRACT

Kinematic and Mechanical Reconstruction of Walker Ridge Structures,

Deepwater Gulf of Mexico. (December 2009)

Oluwatosin Eniola Majekodunmi, B.S., Florida International University

Chair of Advisory Committee: Dr. David V. Wiltschko

Recent high-resolution seismic imaging has allowed detailed reconstruction of the relationship between fold development and crestal faulting of the Chinook and Cascade folds in the deepwater Gulf of Mexico. Using 3-D seismic and biostratigraphic data, we have found that (1) short wavelength (~2300m), small amplitude folds (~540m) within the upper Cretaceous and upper Jurassic stratigraphic sequences took place no later than the late Jurassic, (2) large wavelength and amplitude fold growth, starting in the early Cretaceous, was produced by salt withdrawal, and (3) periods of increased sedimentation, fold growth, and fault slip occurred during the middle Miocene and late Miocene. Although the dominant stage of long wavelength, large amplitude fold growth started around early Cretaceous, the development of the Cascade and Chinook structures was continuous, punctuated by episodes of accelerated growth during the middle Miocene at rates of 337 and 235 m/Ma in the Cascade and 203 and 230 m/Ma in the Chinook. A later event of accelerated growth occurred during the late Miocene at rates of 1038 m/Ma in the Cascade and 1189 m/Ma in the Chinook. Accompanying fold growth was sedimentation, which was highest at 1949 m/Ma in the Cascade and 2585 m/Ma in the Chinook. Although limb tilt rates varied through fold growth, the highest

rates also occurred during the middle Miocene at 0.330 and 0.196 º/Ma for the Cascade and Chinook, respectively with the development of crestal faults at maximum slip rates of 88 and 90 m/Ma.

To the multitude of immigrants around the world misled by those who are supposed to lead, but working for a better life and society

ACKNOWLEDGEMENTS

My appreciation goes to my committee chair and mentor, Dr. David Wiltschko for his guidance and friendship. I would like to thank members of my advisory committee; Dr. John H. Spang and Dr. William R. Bryant for their attention and feedback during the different phases of my project.

I would also like to thank WesternGeco, Bill Kilsdonk and Hess Corporation for making data available for use in this thesis. I thank Zhiyong He of ZetaWare Incorporated whose generosity enabled me to perform structural modelling for my work. Additionally, my thanks go to the Office of Graduate Studies, and Geology and Geophysics Department for providing financial support throughout my study at Texas A&M.

Special thanks go to my mother for her unwavering support, belief in me and love, and to my sister and brother for their encouragement and kindness.

TABLE OF CONTENTS

Page

ABSTRACT iii

DEDICATION v

ACKNOWLEDGEMENTS vi

TABLE OF CONTENTS vii

LIST OF TABLES viii

LIST OF FIGURES ix

INTRODUCTION 1

Background 4

METHODS 6

Dataset 6

Seismic Interpretation 6

Stratigraphy 7

Reconstruction 10

EVOLUTION 16

Pregrowth and Salt Deposition (Triassic-L. Middle Jurassic) 16

Syn-Deposition/Fold Growth (Late Jurassic-Early Pliocene) 16

Post Kinematic Deposition (Early Pliocene-Present) 17

DISCUSSION 18

CONCLUSIONS 22

REFERENCES CITED 24

APPENDIX A 28

APPENDIX B 34

VITA 61

LIST OF TABLES

Page

Table 1. Depth and porosity calculated for intervals 2-12 28

Table 2. Fold and tilt rates for the Cascade and Chinook 29

Table 3. Sedimentation rates calculated for the Cascade and Chinook folds..... 30

Table 4. Area and depth to detachment calculation for section A-A' 31

Table 5. Area and depth to detachment calculation for section B-B' 32

Table 6. Dips of horizons A-J measured from figures 21 and 22 33

LIST OF FIGURES

Page

Figure 1. Graph adapted from Holl and Anastasio (1993) of favored and minimum deformation rates for the Mediano anticline, Southern Pyrenees 34

Figure 2. Summary of the evolution of the Mediano anticline, Southern Pyrenees, after Holl and Anastasio (1993) 35

Figure 3. (a) Overlapping growth strata, (b) Onlapping growth strata, (c) Sedimentation and fold uplift rates for each growth bed in the Santaren anticline, Bahamas foreland..... 36

Figure 4. Location of the Cascade and Chinook folds, Green knoll diapir and Frampton anticline with surrounding MMS protraction areas in the Deepwater Gulf of Mexico..... 37

Figure 5. Structural map of the Cascade and Chinook folds on the mid-Miocene 38

Figure 6. Seismic response (a), Interpreted seismic horizons and intervals (b,c), Biostratigraphic markers (d), Kinematic interpretation (e), Sequences (f) and Corresponding ages (g)..... 39

Figure 7. Profile A-A' through the Cascade and Chinook folds..... 40

Figure 8. Profile B-B' through the Chinook fold..... 41

Figure 9. Cascade and Chinook folds along section A-A'..... 42

Figure 10. Plot of porosity values calculated from bulk density log data for every 0.15 m depth 43

Figure 11. Porosity vs. depth plot extrapolated for intervals *2* and *3* 44

Page

Figure 12. Sequential restorations of section A-A' through the Cascade and Chinook folds 45

Figure 13. Sequential restorations of section B-B' through the Chinook fold 49

Figure 14. Method for measuring fault displacements across respective intervals. 52

Figure 15. Method for measuring amplification of intervals during fold growth ... 53

Figure 16. Method for measuring limb dips, divided by periods of intervening intervals in deriving limb tilt rates for the Cascade and Chinook folds. 54

Figure 17. Cascade and Chinook rates of (a) slip for selected faults, (b) fold growth, (c) limb tilt and (d) sedimentation 55

Figure 18. Fold area and depth to detachment measured for section A-A' 56

Figure 19. Fold area and depth to detachment measured for section B-B' 57

Figure 20. Fold area and depth to detachment plot for (a) section A-A', (b) section B-B' 58

Figure 21. Evolution of horizon *K* through time across A-A' 59

Figure 22. Evolution of horizon *K* through time across B-B' 60

INTRODUCTION

Folding theory has been successful in predicting the fold wavelength, shape and evolution of layered sequences (e.g., Biot, 1961, 1965; Johnson and Fletcher, 1994). For instance, it is well known that folding is a wavelength selective process in that some wavelengths are amplified faster than others. For the simple case of a single viscous layer embedded in an infinite less viscous medium, there is a dominant wavelength that grows faster than all others. The value of this wavelength depends primarily on the competent layer thickness and to a lesser extent on the viscosity contrast between the competent layer and its surrounding medium. However, the rate at which the fold grows depends more directly on the viscosity contrast. The shape of the resulting fold deviates from a simple sine function if the media or layer are non-linear (e.g., power law viscous or plastic).

Most direct tests of folding theory have matched model results to wavelength spectra (e.g., Sherwin and Chapple, 1968), strain distributions (e.g., Groshong, 1972; Chapple and Spang, 1974) or fold shape. Timing of fold growth is rarely known, and therefore, it is not possible to discriminate among time-dependent rheologies. If timing information were available, it would be possible to use either fold amplification rate or fold shape change, or both, to estimate rheology. My purpose is to develop such a data set. Modelling these data to extract rheology I reserve for the next study.

This thesis follows the style of the *American Association of Petroleum Geologists Bulletin*.

Past attempts in estimating rates of fold growth have indicated that fold growth is not steady. Rowan (1997) found that thrust faulting corresponded with rapid shortening that occurred at an estimated rate of 80m/Ma in the Mississippi Fan foldbelt. Detachment folds first grew slowly followed by folding and thrusting as a result of increased rate of regional shortening. A later stage of slow shortening occurred and was marked by fold growth with little or no faulting.

Holl and Anastasio (1993) determined the Eocene growth, sedimentation and limb tilt rates of a fold in the southern Pyrenees using polarity reversal stratigraphy, (Figures 1 and 2). Angular and progressive unconformities on fold limbs within sediments eroded from moving thrust sheet was used to indicate rapid and slow limb tilt rates respectively. Fold growth was generally slow and constant with limb tilt rates of 2.2°- 4.2°/Ma (Figure 1), attributed to sediment-load driven salt deformation. The interval of slow growth was punctuated by periods of rapid growth with limb tilt estimated at 10°- 40°/Ma (Figure 1) due to tectonic compression from the episodic, westward advance of the Cotiella-Montsec thrust sheet (Figure 2, site1).

Masaferro et al. (2002) combined seismic reflection and biostratigraphic data from growth strata to document fold growth rates of the Santaren anticline in the Bahamas foreland (Figure 3). Allowing for compaction, they observed that sedimentation rates obtained for the anticline were not constant through time. High sedimentation rates occurred at 340 and 290 m/Ma during the Early Miocene and Late Miocene respectively. These periods of high sedimentation rate were separated by a long period of low sedimentation rates of 21 to 81 m/Ma. As with sedimentation rates,

Masaferro et al. (2002) calculated higher uplift rates of 340 and 290 m/Ma for the early Miocene and late Miocene. Between these periods of relatively rapid uplift, the fold experienced either slow or no uplift indicated by beds of constant or variable thickness and that thickness variation depended upon the surface topography. Masaferro et al. (2002) used the point of onlap/offlap to determine the degree of difference between sedimentation and uplift. A point of onlap/offlap closer to the anticlinal crest indicates a lesser difference between sedimentation and uplift. With these results, Masaferro et al, (2002) interpreted the Santaren anticline to be a detachment fold formed with possible subsidence of the adjacent synclines. Masaferro et al. (1999) propose that convergence of the North and South American plates during the Cenozoic led to slow fold growth of the Santaren anticline from the Eocene up until present day.

Other studies have also used growth sediments to work out fold growth rates (Poblet and Hardy 1995, Verges et al. 1996). Poblet and Hardy (1995), estimated deformation rates for the Pico del Aguilla anticline, South Central Pyrenees.

Verges et al. (1996) studied the growth of the Can Juncas fold, located in the Ebro foreland basin of the southern Pyrenees. The Can Juncas fold is interpreted to be a detachment anticline whose early fold growth occurred when sedimentation rates were high. Despite accelerated sedimentation, subsequent growth produced offlap in which uplift rates exceeded sedimentation rate. The fold is the result of south east-directed thrustinng in the Oliana anticline. The results of this study suggest that critical kinematic data necessary to model material properties at the scale of an entire fold may be extracted from detailed timing of structures.

The goal in this research is to use well-dated growth strata to produce a detailed kinematic history of the two folds from the Gulf of Mexico. The two structures studied are Cascade and Chinook folds, in the Walker Ridge protraction area of the Gulf of Mexico (Figure 4). The ultimate goal of the larger study is to place constraints on the rheology of the sediments through time.

Background

The evolution of the Gulf of Mexico has been differentiated into four phases by Salvador, (1991) which we briefly summarise here. The *Early rift phase* occurred from the Late Triassic to Middle Jurassic and was characterised by extension from the breakup of the supercontinent Pangaea, creating normal fault bounded grabens filled with non-marine sediments and volcanics. Together with continued rifting during the Middle Jurassic, the Gulf of Mexico region experienced *crustal attenuation* that yielded basement highs and lows and *salt deposition*. Gradual subsidence possibly in the later part of the rift phase was suggested to have occurred in order to accommodate thick salt deposition. In the late Jurassic, emplacement of the oceanic crust from mantle upwelling occurred, followed by thermal subsidence. Marine transgression occurred in the initial stage of cooling and subsidence of the Gulf of Mexico basin. Together with sedimentation induced *subsidence* of the oceanic crust during the Late Jurassic and Early Cretaceous, the Gulf of Mexico basin began to take a configuration that is synonymous with present day. Between the Late-Middle Jurassic to Early Cretaceous, sedimentary depocenters developed along the margin as a result of basinward tilting of the continental margin (Rowan et al, 2000).

The Chinook and Cascade folds are located in the Farnella Canyon area (Bryant et. al, 2001) in the western Mississippi Fan Fold belt. They are basinward of the frontal allochthonous salt of the Sigsbee escarpment in the Walker Ridge protraction area as defined by the Mineral Management Service (Figure 4). These folds lie about 300 km off the Louisiana coast of the United States and below water depths of around 2500 - 2700 m. The Cascade fold is about 24 km north of the Chinook fold with both folds and associated structures covering an area of approximately 120 km².

METHODS

Dataset

The seismic dataset used for this study was acquired by WesternGeco LLP. It consists of 979 km² of high resolution, pre-stack depth-migrated 3D data with bin dimensions of 5 m and 7.5 m in the inline (NE-SW) and crossline (NW-SE) directions, respectively. The ages of the sediments imaged on the seismic were determined from fossils from wells WR 425#2 and WR 469 #1 shown in Figure 5 (see Stratigraphy, below). Synthetic seismograms and ties between proprietary well logs and the available seismic data provide additional constraints on both ages and horizon picks on the seismograms (Figure 1).

Seismic Interpretation

Interpretation of the seismic reflection dataset was performed using Schlumberger IESX Geoframe software®. Twelve horizons, ten of which were tied to the two wells and 112 large and small displacement faults were interpreted (Figure 6). Fault and horizon interpretations around the Cascade and Chinook structures were picked at every 10^{th} and 40^{th} inline and crossline, respectively of the seismic survey. Every 5^{th} arbitrary line was interpreted in areas of stratigraphic and structural intricacy, whereas every 20^{th} arbitrary line was interpreted elsewhere. The resulting depth structure maps for each horizon were then used to create isopachs. Isopachs between adjacent horizons that we term “interval isopachs” were produced by subtracting successive depth structure maps from each other.

The Cascade and Chinook folds are elliptical domes in map view (Figure 5). These folds trend NE-SW and contain mostly NW-SE striking conjugate normal faults. The fault pattern around the Chinook structure is somewhat radial. In cross section, the structures are open and asymmetric salt cored anticlines (Figure 7 and 8). Both anticlines and the intervening syncline are underlain by deformed Mid Jurassic Louann salt. The salt is thinner beneath the syncline relative to the anticlines. Syn-kinematic interval I displays small wavelength and amplitude folds. The Syn-kinematic II sequences thicken from the anticlinal axial surface towards the intervening syncline. Sedimentary intervals are displaced by normal faults around the anticlines and are thicker in the hanging wall relative the footwall of the fault. A few of these faults displace Post-kinematic strata.

Stratigraphy

Thirteen horizons were mapped on seismic and used to define twelve stratigraphic intervals (Figure 6). The top of a non-reflecting interval below horizon *K* was taken top of the salt. Ages of *A* to *J* (Early Eocene) were determined by Hess Corporation from biostratigraphic indicators in wells WR 425 #2 and WR 469 # 1. Because the remaining two horizons, *K* and *Top salt*, were not penetrated by these two wells, we have followed the regional correlations of Feng and Buffler (1991) based on the seismic character of extensive, continuous, high amplitude reflectors to define *K* and *Top salt*. Pairs of horizons define stratigraphic intervals that we have numbered from *1* to *12*, oldest to youngest (Figure 6).

We have defined intervals as Pre-kinematic, Syn-kinematic (both I and II, see Figure 6) and Post-kinematic based on the presence of growth strata (Syn-kinematic) and involvement in the folding (pre- or post-kinematic). Interval *1*, is the interpreted pre-kinematic interval, *2* to *12* are syn-kinematic and all units younger than *12* are largely post-kinematic.

The Pre-kinematic interval is characterized by high amplitude and relatively parallel seismic reflectors. This interval ranges in thickness between 0.3-1.5 km. Low amplitude, random seismic reflectors of the deformed Middle Jurassic salt overlie the Pre-kinematic interval and pinches out between the Pre-kinematic and Syn-kinematic I intervals. The Syn- kinematic interval I is characterized by small wavelength and amplitude folds with dimensions of 2300 m and 540 m, respectively, with thickness ranging between 0.5-1 km. High amplitude seismic reflectors mark the upper boundary of this interval.

The Syn-kinematic II interval accounts for most of the thickness of units making up the Chinook and Cascade folds. These sequences exhibit sedimentary expansion away from the hinge of the anticlines with thickness ranging between 3.5km at the anticlinal axial surface to 5km in the syncline. Middle to upper Miocene strata (intervals 7 to 12) show significant increase in thickness to the SW and NW of the Cascade and Chinook, respectively (Figure 7 and 8). Intervals 3 to 6 between the lower Cretaceous and Oligocene appear relatively constant in thickness but still exhibit thickening on the western limb of Chinook. Older units within interval 3 onlap against horizon K (Insert Figure 7b). Additionally, interval 3 shows greater thickness on the SE limb relative to

the NW limb (Figure 7), opposite to the general trend of greater thickness on the NW limbs for all other syn-kinematic intervals. The Post-kinematic interval ranges in thickness between 3.2-3.5 km and displays seismic reflectors that onlap against horizon A. (Figure 9).

The lithologic descriptions below are based on interpretations from well data from Weimer and Buffler (1992) for stratigraphic sequences in the Mississippi Fan foldbelt. The Challenger sequence (Figure 6) is interpreted to overlie the basement, containing sediments of middle Jurassic to lower Upper Cretaceous. This sequence is interpreted to contain salt near the base followed by shallow marine carbonates, deep marine carbonates and shale. Separating the Challenger and Campeche sequence is the Middle Cretaceous Sequence Boundary (MCSB). The Campeche sequence contains deposits of upper Cretaceous to lower Tertiary age with lithology interpreted to consist of mostly deepwater shales and chalk.

The Lower Mexican Ridges sequence consists of deepwater shales and chalks of lower Tertiary to upper Oligocene whereas the middle Mexican Ridges sequence consists of Upper Oligocene to Middle Miocene deepwater shales and marls. Weimer and Buffler (1992), report that the Upper Mexican Ridges sequence is composed of unchannelized, coarse grained deepwater turbidites of middle to upper Miocene age. Lastly, the Mississippi Fan sequence is interpreted to consist of upper Miocene to Quaternary age channel levee deposits.

Reconstruction

Decompaction

The seismic interpretation is the starting point for reconstructing the kinematics of the folds. To accurately represent the fold geometry at each stage of development, the interval thicknesses must be returned to their values at each stage in the folds' development.

Present day porosities were measured from well log data together with formation tops containing depths at which the well penetrated horizons which we obtained from Hess Corporation. Since our well data contained bulk density curves, we assumed the densities for the matrix and fluid in our intervals and calculated porosities (ϕ_d) using the relationship below:

$$\phi_d = \frac{\rho_m - \rho_b}{\rho_m - \rho_f} \quad (1)$$

ρ_b: bulk density from log curve, ρ_f : fluid density which we assigned to be 1 gcm^{-3}, and ρ_m: density of matrix containing mostly shale with an assumed value at 2.68 $gcm^{-3.}$

Figure 10 shows the plot of porosity measured every 0.5 feet (0.15 metres) within the folded units. By averaging porosities between successive formation tops corresponding to our horizons, we were able to derive an average porosity for intervals *4* to *12*. Because no well data exist for intervals *2* and *3,* we use formation tops to extrapolate their porosities from the porosity vs. depth plot for intervals *4* to *12* (Figure

11). Factors that may limit porosity such as mineral transformations, cementation and fluid expulsion (Petersen, 1991) were not considered.

The process of decompaction was performed using the porosity and depth relationship based on Sclater and Christie (1980):

$$\phi = \phi_o e^{-cy} \quad (2)$$

where ϕ is present day porosity at depth *y* (See Table 1), ϕ_o is the surface porosity derived from the intercept of the slope on the porosity axis which gives a value of 0.5 and *c* is porosity-depth coefficient which is the slope (0.17 km^{-1}) of the line in Figure 11.

2D restoration

Each interval was sequentially restored by (1) decompacting intervals and those below, (2) unfolding using flexural slip and (3) reversing displacements along fault surfaces. Interval geometries and structures were digitised from seismic sections shown in Figure 7 and 8 to perform a two dimensional restoration of folded structures. Twelve stages of restoration, each for intervals *1* to *12*, were performed for the Cascade and Chinook folds.

The restorations in Figure 12 and 13 show pre-existing sediments over the basement prior to the arrival of salt. Salt was not considered to be compactable material during the process of restoration and assumed to have moved into the area of section.

Fault slip

We selected faults that displaced at least three horizons. The fault slip of an interval was assigned as the measured displacement of its lower bounding horizon along the plane of the fault (Figure 14). Since we are concerned with rates, all displacements measured were divided by the time period within an interval displaced by a fault to derive the slip rates within intervals.

Rates in most faults showed higher fault slip rates for intervals *7* and *10* relative to other intervals. The highest rates calculated occurred within intervals *7* and *10* at maximum rates of 88 and 90 m/Ma, respectively.

Fold growth

The rate of fold growth for the Chinook and Cascade was estimated from each stage of the sequential restoration. The amplitude of the uppermost folded horizon at each level of fold growth is the vertical distance from the level of the abyssal plain (towards A' and B' in Figure 7 and 8), to the anticlinal crest. The amplitudes (*A*) derived for each interval of fold growth is then divided by the corresponding time period (*t*) to get the rates (Figure 15).

The rates in the Cascade fold steady from intervals *1* to *6*, followed by major increases within intervals *7* and *10* at estimated rates of 337 and 235 m/Ma respectively. The Chinook fold also experienced a comparatively low and steady rate from intervals *1* to *6,* followed by a similar jump in intervals *7* and *10* at rates of 203 and 230 m/Ma. The highest rates for both Cascade and Chinook occurred in interval *12*, at rates of 1038 and

1189 m/Ma, respectively (Table 2). The high rates derived for interval *12* suggests there was considerable increase in fold amplitude within a short period of time (0.26 Ma).

Limb tilt

An estimation of limb dip measurements was made by measuring the dip of a line joining the anticlinal and synclinal hinges. (Figure 16). While this an incorrect measure of limb dip, this measured proved more convenient than estimating the location of the inflection point which lies near the synclinal hinge. The results are in Table 2.

Figure 17 c shows variation in tilt rates for the Cascade and Chinook folds. Limb tilt rate in the Chinook is highest at ~0.33°/Ma in interval 7 while tilt rate in the Cascade is highest at ~0.20°/Ma in interval 10.

Sedimentation

Sedimentation rates were estimated to assess how sedimentation kept pace with fold growth. These calculations were performed on abyssal plain sediments (right ends of sections in Figures 7 and 8 respectively) because they are undeformed. The decompacted thicknesses were divided by the time represented by the interval to yield the sedimentation rate.

Figure 17d shows that higher sedimentation rates correspond to accelerated growth of the Cascade fold. The intervals of highest sedimentation rate are 427, 256 and 1949 m/Ma in intervals *7*, *10* and 12 respectively. The peak sedimentation rates in the Chinook fold also occurred in intervals *7,10* and *12* (522, 419 and 2585 m/Ma, respectively; see Table 3).

Area and depth to detachment

We applied the area-depth to detachment method by Epard and Groshong (1993) to section A-A' and B-B' to understand the depth of folding and growth kinematics of the Cascade and Chinook folds. The reference for the calculation was the base of salt observed on seismic about 11.5 km depth. For each sedimentary horizon above salt, we used the horizon's abyssal plain level as its reference line (Figure 18 and 19). The depth to detachment for each horizon was then measured as the vertical distance between the base salt level and the horizon's reference. Fold area for each horizon in the anticlines and synclines measured for horizons *A* to *K* were treated as positive and negative respectively (Tables 4 and 5). Anticlinal areas were halved to correspond with half synclines measured from the seismic cross sections.

The anticlinal fold area decreases up section (Figure 20a, b). Causes for such trend could be related to cumulative of fold growth by limb lengthening. In figure 20a, the synclinal fold area appears to decrease from *K* to *J* and then increase in *I* before gradually decreasing in younger horizons up to *A*. The synclinal fold area increases from intervals *K* to *J* and gradually decreases to *H* indicating movement of salt volume into the syncline before the onset of salt withdrawal towards the anticline at the time of *H* (Figure 20b).

Paleostructure

Structural maps through time were created for horizon *K*. The average depth of the abyssal plain in the structural map of horizon *K*, located at the south eastern edge of our study area was used as reference. The average depth of *K* was then subtracted from

the structural map values of each successive horizon (*A*-*J*). For example, the difference between the present day structural map value of horizon *J* and the average value of the abyssal plain from the structural map of horizon *K* would yield a palaeostructural map of horizon *K* at the time of *J* (49.9 Ma). The resulting paleostructure, displayed for sections A-A' (Figure 21) and B-B' (Figure 22), depicts the growth of horizon *K* from the time of horizon *J* during the early Eocene up to the time of horizon *A* (5.54 Ma) in the late Miocene. Although limb tilt rates varied (Figure 17c), Figures 21 and 22 show increasing limb dip and lengthening of horizon *K* through fold growth. Additionally, a significant increase in structural relief of the synclines takes place within both folds from the Eocene (horizon *J*) to the Oligocene (horizon *I*).

EVOLUTION

Pregrowth and Salt Deposition (Triassic- L. Middle Jurassic)

Following the late Triassic rifting of the Gulf of Mexico basin was the deposition of interval *1*. This interval is characterised by continuous, roughly parallel seismic reflectors. Each reflector does not appear to intersect or meet adjacent reflectors. The bottommost reflector is assumed to overlay the basement. This event was capped by the deposition of salt (Figure 12(m) and 13(m)).

Syn-Deposition/Fold Growth (Late Jurassic- Early Pliocene)

The syn-kinematic stage was characterized by the several phases of deposition and deformation within the period of intervals *2-12*. Interval *2* was deposited and deformed into small amplitude and wavelength folds (Figure 12(l) and 13(l)), possibly a result of down dip contraction induced by up dip extension.

The deposition of interval *3* was followed by fold growth that occurred from 65.5 to 49.9 Ma (Early Cretaceous to the Late Eocene). We tied this event to the observation of significant thickness in interval *3* on the eastern limb relative to the western limb of the Chinook fold, where older units within interval *3* onlap against horizon *K*. We propose that the start of deposition of interval *2* caused deformation of salt that in turn yielded a structural high just NW of the abyssal plain (Figure 12(m) and 13(m)). An occurrence of non-deposition towards the abyssal plain is indicated by local onlap (Figure 7b insert). It was during this time of relative sediment starvation that faulting began. Accompanying the arrival of interval *4* was a decrease in the rate of fold growth

and faulting. As with succeeding intervals, fold growth was accomplished by salt motion from the synclines into the anticlines.

The deposition of interval *5* marked increased rates of folding and faulting relative to the previous units (Figure 12(i) and 13(i)). While fault and fold rates increased through interval *6*, both peaked during interval *7*. The accelerated rates of fold growth in the Chinook and Cascade folds corresponded with an increase in the number of crestal faults displacing units within the interval.

The Chinook and Cascade folds continued to develop through the Miocene with the deposition of intervals *8* through *12* although folding and faulting peaked again during the middle and late Miocene at intervals *10* and *12*. Intervals of higher sedimentation were synchronous with accelerated folding and major faulting. Although fault slip and limb rotation rates slowed during interval *12*, periods of accelerated fold growth, fault slip, limb tilt and sedimentation coincide, suggesting the deformation of the underlying salt played a major role.

Post Kinematic Deposition (Early Pliocene - Present)

Rapid sedimentation began between the late Miocene and early Pliocene with erosion signalling the end of the folding. As a result, units onlap above interval *12* (Figure 9 insert), showing parallel seismic reflectors above hinges of both folds. Moreover, crestal faults that dominated the syn-kinematic intervals did not displace strata younger than the Early Pliocene.

DISCUSSION

Weimer and Buffler (1992) suggest that the present limit of the Mississippi Fan foldbelt is located at the basinward limit of salt. In this view, shifts in sediment load distribution had controlled positions of depocentres and consequently the location of folding. Wu and Bally (1990) further suggest that shifts in the drainage systems that supplied sediments to the Gulf of Mexico controlled the timing of extension, salt deformation and down-slope contraction. Specifically, deformation of salt caused lateral displacement of Mesozoic-middle Miocene units toward the basinward limit of salt. The pre-existing salt deposition pattern therefore controlled the locations of subsequent folding.

From the analysis of growth sequences on fold limbs and sequential restoration of frontal folds in the Mississippi fan foldbelt, Rowan (1997) proposes the following growth stages: (1) An early stage of detachment folding over pre-existing salt pillows from the late Oligocene to early Miocene, (2) thrust faulting through fold forelimbs during the middle Miocene and (3) fold amplification from the late Miocene to Pliocene during which faults did not develop further.

Likewise, Grando and McClay (2004) propose for the Frampton anticline in the Gulf of Mexico the following events: (1) Salt swells and ridges associated with basement rifting, (2) small wavelength salt pillows during the L. Jurassic-Cretaceous, (3) salt diaprism, followed by fold growth during the L. Miocene- E. Pliocene, (4) burial of the fold by Mississippi fan sediments between L. Pliocene-Pleistocene.

Vendeville and Jackson (1992) suggest that the difference between salt-cored anticlines and diapirs is the thickness and strength of the overburden. To prevent diapirism the overburden must both exceed a critical thickness and be strong enough to prevent salt diapir penetration. Mechanisms that reduce the strength or thickness of the overburden such as faulting and erosion could favour diapirism. Although the mechanism is not entirely clear, several studies of fold kinematics have demonstrated that folding is accompanied by, and perhaps caused by, increased sedimentation.

Verges et.al (1996) demonstrated for the Can Juncas anticline of the Ebro foreland basin that onlap during early fold growth (36.38- 35.37 Ma) resulted from sedimentation rates (~80 m/Ma) exceeding uplift (~50 m/Ma). Despite accelerated sedimentation (160 m/Ma), offlap occurred between 35.37 and 34.96 Ma because of higher uplift rate (220 m/Ma) during which most of the fold height was achieved by forelimb rotation at the rate of 8 $x10^{-4}$ °/Ma. From 34.96 to 34.67 Ma, rapid shortening (460 m/Ma), limb rotation increased (2 $x10^{-3}$ °/Ma) and uplift of growth strata exceeding sedimentation occurred to produce offlap.

Poblet and Hardy (1995) assumed fold growth model by limb rotation and estimated thrust displacement together with fold amplification rates to determine the kinematic evolution of the Pico del Aguila anticline, the South Central Pyrenees. Constant shortening (350 m/Ma) during growth of constant limb length folds would yield decreasing uplift rates, adding that beds deposited at the later stage of fold growth will show little thickness variations due to low uplift. With variable limb length fold model, estimated shortening rates decreased from a maximum of 990 m/Ma and a

decrease in uplift from an initial rate of about 310 m/Ma. With these trends, Poblet and Hardy (1995) proposed that during folding, constant limb folds accommodate shortening by limb rotation while variable limb length folds accommodate shortening by limb rotation and lengthening.

Cartwright et al. (1998) concluded that faulting within recent Gulf of Mexico deposits (late Pleistocene to Holocene) are driven by sedimentary loading. Analysis of fault slip versus depth for the faults studied showed cycles activity which they attributed to cyclicity in sedimentation. However, the periodicity of some individual faults was out of phase with adjacent faults, suggesting local differences in sediment loading.

The crestal normal faults that characterise the Cascade and Chinook folds may have developed from bed extension during salt motion into the anticlines. Although two periods of increased sedimentation and fault slip occurred in the middle Miocene, the same did not occur in the late Miocene where fault activity lessened while sedimentation rates were highest. From palaeostructural analysis in Figure 21 and 22, we have shown that the present day bed lengths are much longer than their original lengths and propose that faulting ceased when the salt underlying the syncline was effectively depleted.

It is apparent that the present geometry of the Cascade and Chinook folds developed during periods of more rapid sedimentation. Despite variation in rates, sedimentation in the Cascade and Chinook exceeded fold growth rates during deposition with all units within the Syn-kinematic intervals exhibiting overlap across the anticlinal hinge. The higher rates occurred in the mid Miocene (427, 256 m/Ma in the Cascade, 522 and 419 m/Ma in the Chinook), while rates were highest in the late Miocene (1949

and 2585 m/Ma) for the Cascade and Chinook folds, respectively. Previously suggested rates in the deepwater Gulf have varied, i.e., 50-280 m/Ma in Pleistocene sediments (Elston, 2005) and 160- 910 m/Ma between the Late Oligocene and Late Miocene (He et.al, 2006). The only exception is the onlap of older units of interval *3* against horizon *K* (Figure 7b insert). Horizon *K* in our data was represented as the Mid Cretaceous Sequence Boundary by Addy and Buffler, (1984) while Wu et al. (1990) indicated that the Mid Cretaceous Sequence Boundary may have represented a flooding surface in the deep Gulf of Mexico Basin. As a result, the observed onlap might indicate renewed sedimentation after flooding.

The progressive decrease in the dip of successively younger horizons of the present day Cascade and Chinook folds imply continued fold growth (Figure 21 and 22). Two distinct episodes of accelerated limb tilt occurred during the middle Miocene with the highest rates at 0.20 and 0.18 °/Ma in the Cascade and 0.33 and 0.24 °/Ma in the Chinook before gradually decreasing towards the late Miocene (Figure 17 c). Overlap geometry displayed in the Syn-kinematic units (Figure 7 and 8) suggest that sediment thickness exceeded the existing structural high throughout fold growth, particularly in interval *12*, regardless of limb tilt rate variations.

CONCLUSIONS

- The Cascade and Chinook are NE trending asymmetric anticlines that are cored by Middle Jurassic Louann salt and contain normal faults within the crests. Both folds are separated by a syncline that is underlain by tectonically thinned salt.
- An early phase of small wavelength and amplitude fold growth took place no later than the late Jurassic. At this time the sedimentary overburden over the salt was approximately 700 metres.
- A later phase of increased fold growth rate occurred with the deposition of growth sediments that thinned over the crest of anticlines and were displaced by normal faults.
- Fold growth and fault slip are not steady. Two events of accelerated growth occurred in the middle at 337 and 235 m/Ma for the Cascade, while rates were at 203 and 230 m/Ma in the Chinook fold. A later event of accelerated fold growth occurred in the late Miocene at 1038 and 1189 m/Ma for the cascade and Chinook folds, respectively. Fold growth eventually ceased during the early Pliocene. The periods of fastest fault motion occurred in the middle Miocene at rates of 88 and 90 m/Ma.
- Accelerated fold growth coincided with intervals of more rapid sedimentation in the Cascade fold (427 and 256 m/Ma in the middle Miocene and 1949 m/Ma in the late Miocene). For the Chinook fold, accelerated sedimentation occurred at 522 and 419 m/Ma in the middle Miocene and 2585 m/Ma in the late Miocene.

- Tilt rates varied during fold growth. Accelerated tilt rates occurred in separate periods during the middle Miocene at maximum rates approximately 0.181 and 0.196 °/Ma in the Cascade, and 0.330 and 0.243 °/Ma in the Chinook.
- The Cascade and Chinook anticlinal hinges were fixed very early in the folds' evolution with no substantial change in position with continued deformation.

REFERENCES CITED

Addy, S.K. and R.T. Buffler, 1984, Seismic stratigraphy of shelf and slope, northeastern Gulf of Mexico: AAPG Bulletin, v. 68, p. 1782-1789.

Biot, M.A., 1961, Theory of folding of stratified viscoelastic media and its implications in tectonics and orogenesis: Geological Society of America Bulletin, v. 72, p. 1595-1620.

Biot, M.A., 1965, Theory of similar folding of the first and second kind: Geological Society of America Bulletin v. 76, p. 251-258

Bryant, W.R., D. Bean, N. Slowey, T. Dellapenna and E. Scott, 2001, Deepwater currents from mega-furrows near US Gulf's Sigsbee Escarpment. Offshore, v. 61, p. 94-95.

Chapple, W.M and J.H. Spang, 1974, Significance of layer-parallel slip during folding of layered sedimentary rocks: Geological Society of America Bulletin v. 85, p. 1523–1534.

Elston, K.E., 2005, A chronostratigraphic framework for the Northwestern Slope of the Gulf of Mexico. M.S. Thesis, Texas A&M University.

Epard, J.-L., and R.H. Groshong, 1993, Excess area and path to detachment: AAPG Bulletin, v. 77, p. 1291-1302.

Feng, J., and R.T. Buffler., 1991, Preliminary age determinations for new deep Gulf of Mexico basin seismic sequences: Transactions -Gulf Coast Association of geological Societies proceedings, v. 41, p. 283-289.

Grando, G., and K. McClay, 2004, Structural evolution of the Frampton growth fold system, Atwater Valley– southern Green Canyon area, deep water Gulf of Mexico: Marine and Petroleum Geology, v. 21, p. 889-910.

Groshong, R.H., 1972, Strain calculated from twinning in calcite: Bulletin of the Geological Society of America v.82, p. 2025–2038.

He, L., N. Dawers, and C. Stelting, 2006, Post-30-M.y. Sequence Stratigraphy, Northeastern Gulf of Mexico. AAPG Annual Convention Abstract.

Holl, J.E., and D.J. Anastasio, 1993, Paleomagnetically derived folding rates, Southern Pyrenees, Spain: Geology, v. 21, no. 3, p. 271-274.

Johnson, A.M., and R.C. Fletcher, 1994, Folding of viscous layers, Columbia University Press, New York, p. 1-461.

Masaferro, J.L., M. Bulnes, J. Poblet, G.P. Eberli, 2002, Episodic folding inferred from syntectonic carbonate sedimentation: the Santaren anticline, Bahamas foreland: Sedimentary Geology, v. 146, p. 11-24.

Masaferro, J.L., M. Bulnes, J. Poblet, G.P. Eberli, T.H. Dixon, K. McClay, 1999, Palaeogene-Neogene/present day growth folding in the Bahamian foreland of the Cuban fold and thrust belt: Journal of the Geological Society, London, v. 156, p. 617-631.

Petersen, K., 1991, The effect of gravitational compaction on estimation of vertical salt structure growth: Tectonophysics, v. 194, p. 35-48.

Poblet, J., and S. Hardy, 1995, Reverse modelling of detachment folds: application to the Pico de Aguila anticline in the South Central Pyrenees, Spain: Journal of Structural Geology, v. 17**,** p. 1707–1724.

Rowan, M. G., 1997, 3-D geometry and evolution of a segmented detachment fold, Mississippi Fan fold belt, Gulf of Mexico: Journal of Structural Geology, v. 19, p. 463-480.

Rowan, M. G., B. D. Trudgill, and J. C. Fiduk, 2000, Deepwater, salt-cored fold belts: Lessons from the Mississippi Fan and Perdido fold belts, northern Gulf of Mexico, *in* W. Mohriak and M. Talwani, ed., Atlantic rifts and continental margins: American Geophysical Union Geophysical Monograph, v.115, p. 173-191.

Salvador, A., 1991, Origin and development of the Gulf of Mexico basin, *in* Salvador, A., ed., The Gulf of Mexico basin: Boulder, Colorado, Geological Society of America, The Geology of North America, v. J, p. 389-444.

Sclater, J.G., and P.A.F. Christie, 1980, Continental stretching: An explanation of the post-Mid-Cretaceous subsidence of the Central North Sea Basin: Journal of Geophysical Research, v. 85, no. B7, p. 3711-3739.

Sherwin, J.A., and W.N. Chapple, 1968, Wavelengths of single layer folds: A comparison between theory and observation: American Journal of Science, v.266, p. 167–179.

Weimer, P., and R. Buffler, 1992, Structural geology and evolution of the Mississippi Fan Fold Belt, deep Gulf of Mexico: AAPG Bulletin, v. 76, p. 225-251.

Vendeville, B. C., and M. P. A. Jackson, 1992, Critical roof thickness of active diapirs: EOS Transactions, American Geophysical Union, v. 73, no. 27, p. 572

Vergés, J., Burbank, A.W., and Meigs, A., 1996, Unfolding: An inverse approach to fold kinematics: Geology, v**.** 24, p. 175–178.

Wu, S., P.R. Vail, and C. Cramez, 1990, Allochthonous salt, structure and stratigraphy of the northeastern Gulf of Mexico. Part I: Stratigraphy: Marine and Petroleum Geology, v. 7, no. 4, p 318-333.

Wu, S., and A. W. Bally, 1990, Slope Tectonics- Comparisons and Contrasts of Structural Styles of Salt and Shale Tectonics of the Northern Gulf of Mexico with Shale Tectonics of Offshore Nigeria in Gulf of Guinea: Geophysical Monograph, American Geophysical Union, v. 115, p. 151-172.

APPENDIX A

Table 1. Depth and porosity calculated for intervals 2-12.

Interval	*Depth (km)*	*Porosity*
12	5.66	0.25
11	5.82	0.20
10	6.34	0.192
9	6.54	0.148
8	6.59	0.166
7	6.85	0.125
6	7.03	0.172
5	7.38	0.135
4	7.44	0.12
3	8.83	0.11
2	9.60	0.095

Table 2. Fold and tilt rates for the Cascade and Chinook.

		CASCADE		*CHINOOK*	
Interval	***Period (Ma)***	***Fold rate (m/Ma)***	***Tilt rate (°/Ma)***	***Fold rate (m/Ma)***	***Tilt rate (°/Ma)***
12	0.26	1038	0.099	1189	0.085
11	5.20	58	0.102	26	0.130
10	0.90	235	0.196	230	0.210
9	0.90	118	0.133	116	0.243
8	2.00	60	0.102	42	0.197
7	0.80	337	0.181	203	0.330
6	6.30	27	0.116	33	0.129
5	1.90	52	0.097	47	0.098
4	26.1	3.8	0.145	19.5	0.069
3	15.6	17	*N/A*	27	*N/A*
2	93.5	3.6	*N/A*	8	*N/A*

Table 3. Sedimentation rates calculated for the Cascade and Chinook folds.

	CASCADE	*CHINOOK*
Horizon	***Sedimentation rate (m/Ma)***	***Sedimentation rate (m/Ma)***
12	1949	2585
11	95	160
10	256	419
9	104	143
8	218	378
7	427	522
6	96	110
5	57	52
4	40	32
3	95	67
2	18	16

Table 4. Area and depth to detachment calculation for section A-A'. H is the depth to detachment, A is the anticlinal fold area, -A is the synclinal fold area and ΣA is the net area.

Horizon	*H(km)*	*A(km^2)*	*-A(km^2)*	*ΣA(km^2)*
A	5.47	0.863	-1.340	-0.477
B	5.06	0.845	-3.092	-2.247
C	4.64	1.084	-4.269	-3.185
D	4.42	1.299	-4.853	-3.553
E	4.35	1.214	-4.872	-3.659
F	4.02	1.506	-5.971	-4.465
G	3.75	1.757	-6.105	-4.349
H	3.27	2.086	-6.805	-4.719
I	3.19	2.131	-6.709	-4.580
J	2.47	3.066	-6.703	-3.637
K	1.30	4.547	-4.721	-0.175

Table 5. Area and depth to detachment calculation for section B-B'. H is the depth to detachment, A is the anticlinal fold area, -A is the synclinal fold area and ΣA is the net area.

Horizon	*H(km)*	*A(km^2)*	*-A(km^2)*	*ΣA(km^2)*
A	6.48	1.029	0	1.029
B	6.11	1.244	-0.430	0.814
C	5.66	1.557	-1.034	0.523
D	5.49	1.756	-1.249	0.507
E	5.42	1.739	-1.255	0.484
F	5.13	2.176	-1.618	0.558
G	4.88	2.535	-1.686	0.849
H	4.39	3.084	-1.991	1.093
I	4.32	3.271	-2.207	1.064
J	3.57	4.539	-1.793	2.746
K	2.57	6.095	-1.988	4.107

Table 6. Dips of horizons A-J measured from figures 21 and 22.

	CASCADE	*CHINOOK*
Horizon	***Dip (⁰)***	***Dip (⁰)***
A	12.39	11.42
B	12.36	11.40
C	11.83	10.72
D	11.65	10.53
E	11.53	10.31
F	11.33	9.916
G	11.18	9.652
H	10.45	8.840
I	10.27	8.654
J	6.477	6.862

APPENDIX B

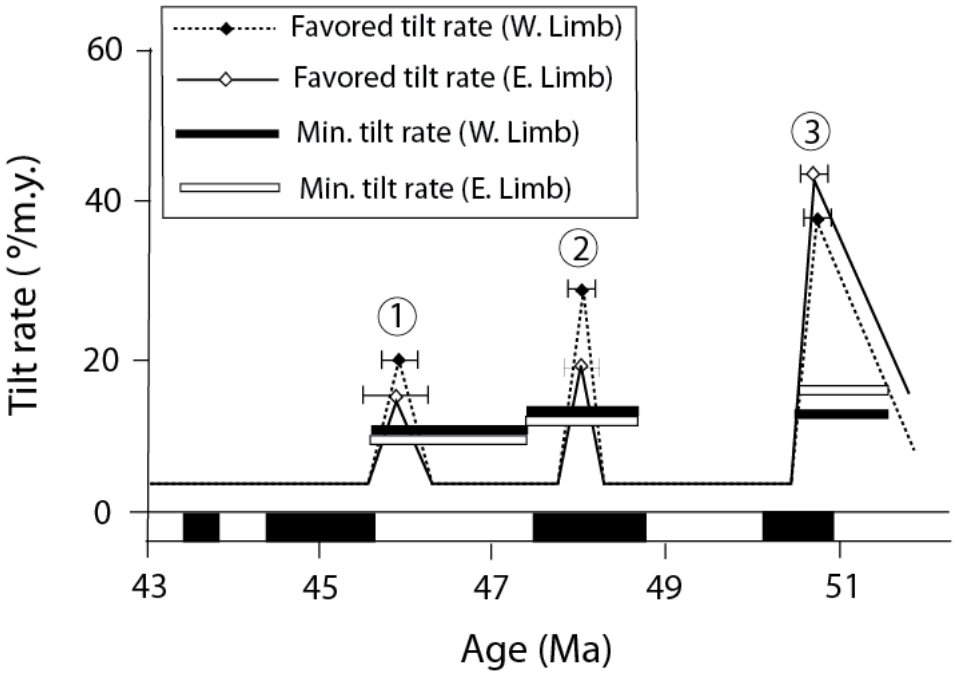

Figure 1. Graph adapted from Holl and Anastasio (1993) of favored and minimum deformation rates for the Mediano anticline, Southern Pyrenees. Geomagnetic reversal time scale is shown on the horizontal axis; angular unconformities are identified by circled numbers.

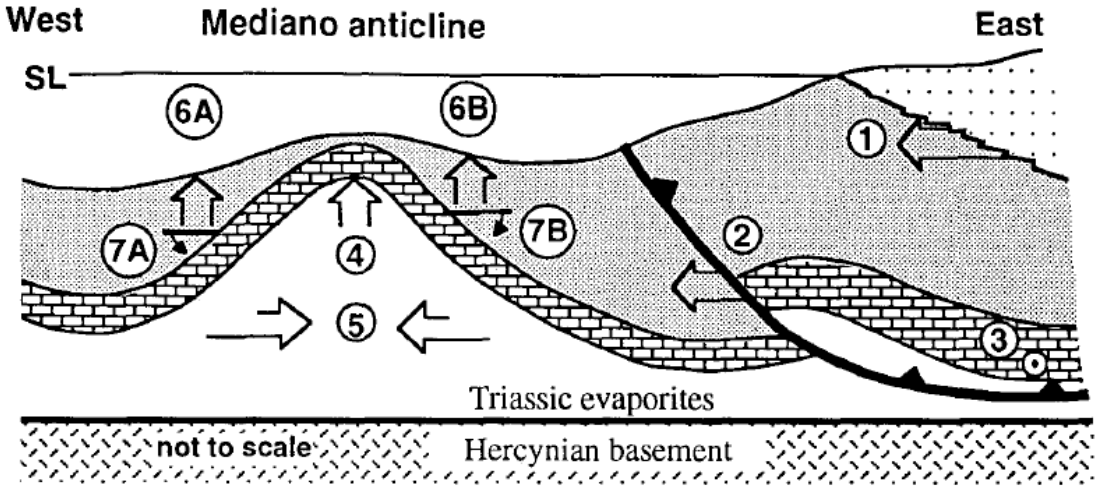

Figure 2. Summary of the evolution of the Mediano anticline, Southern Pyrenees, after Holl and Anastasio (1993). Circled numbers represent events and average rates in fold growth and surrounding structures. (1) Westward continental facies progradation at 500 m/Ma. (2) Westward component of thrust sheet motion (200 m/Ma). (3) Southward component of thrust-sheet motion (900 m/Ma). (4) Crestal uplift: (250 m/Ma). (5) Horizontal shortening of anticline (500 m/Ma). (6A) Sedimentation rate for westward fold limb (200 m/Ma). (6B) Sedimentation rate for eastward fold limb (70 m/Ma). (7A) Westward limb tilt (6.5°/Ma). (7B) Eastward limb tilt (7.5°/Ma).

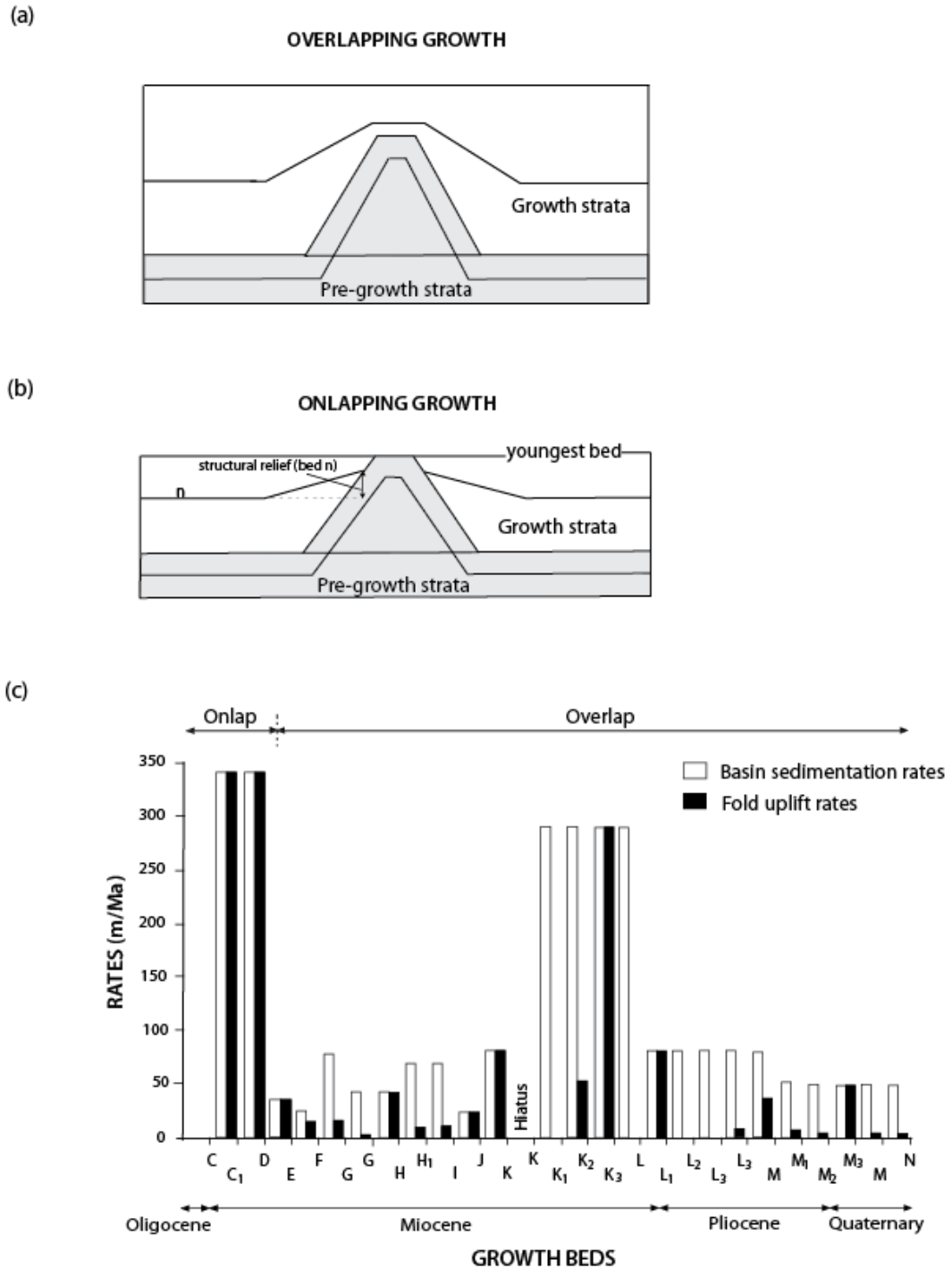

Figure 3. (a) Overlapping growth strata, (b) Onlapping growth strata, (c) Sedimentation and fold uplift rates for each growth bed in the Santaren anticline, Bahamas foreland. C, C_1, D....etc are lithologic units as defined by Masaferro et al., (2002).

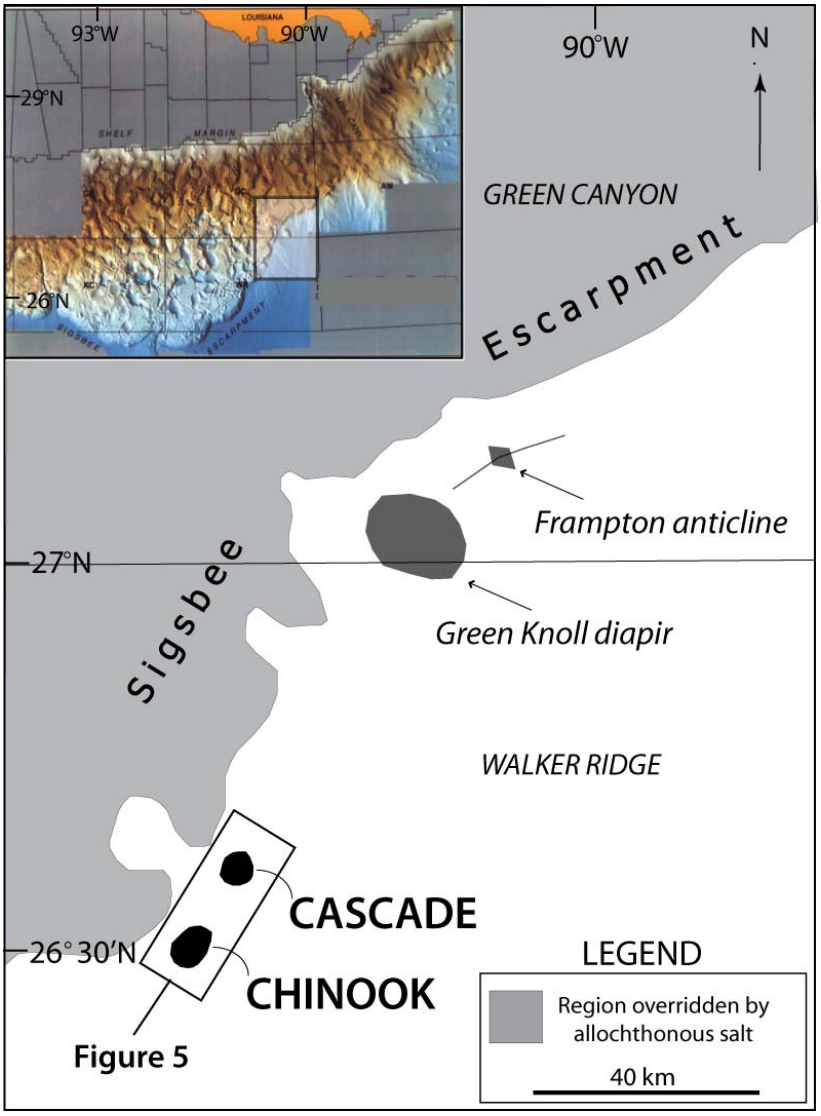

Figure 4. Location of the Cascade and Chinook folds, Green knoll diapir and Frampton anticline with surrounding MMS (Mineral Management Service) protraction areas (Walker Ridge and Green Canyon) in the Deepwater Gulf of Mexico. Modified after Grando and McClay (2004).

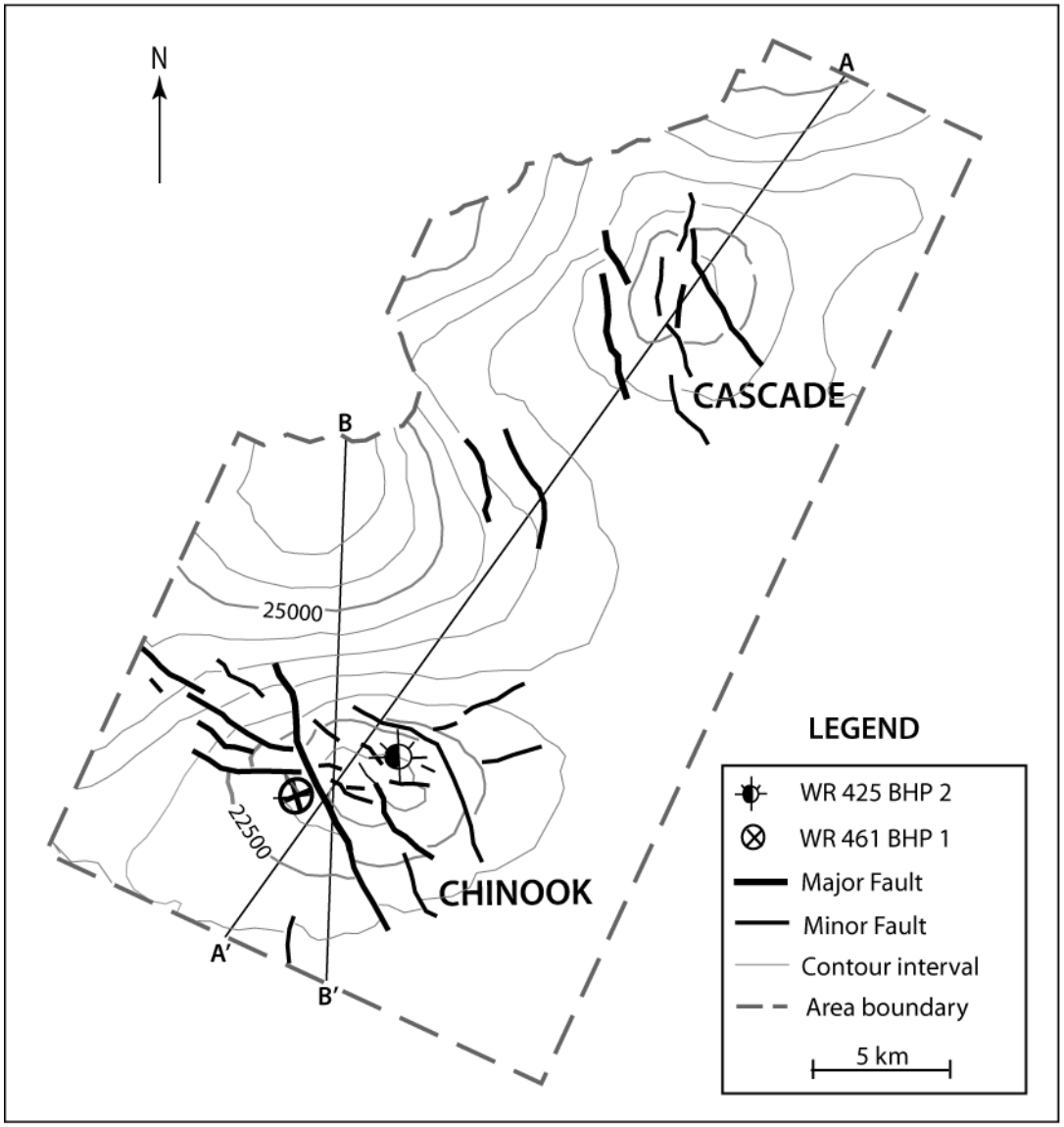

Figure 5. Structural map of the Cascade and Chinook folds on the mid-Miocene (Horizon E, see Figure 6).

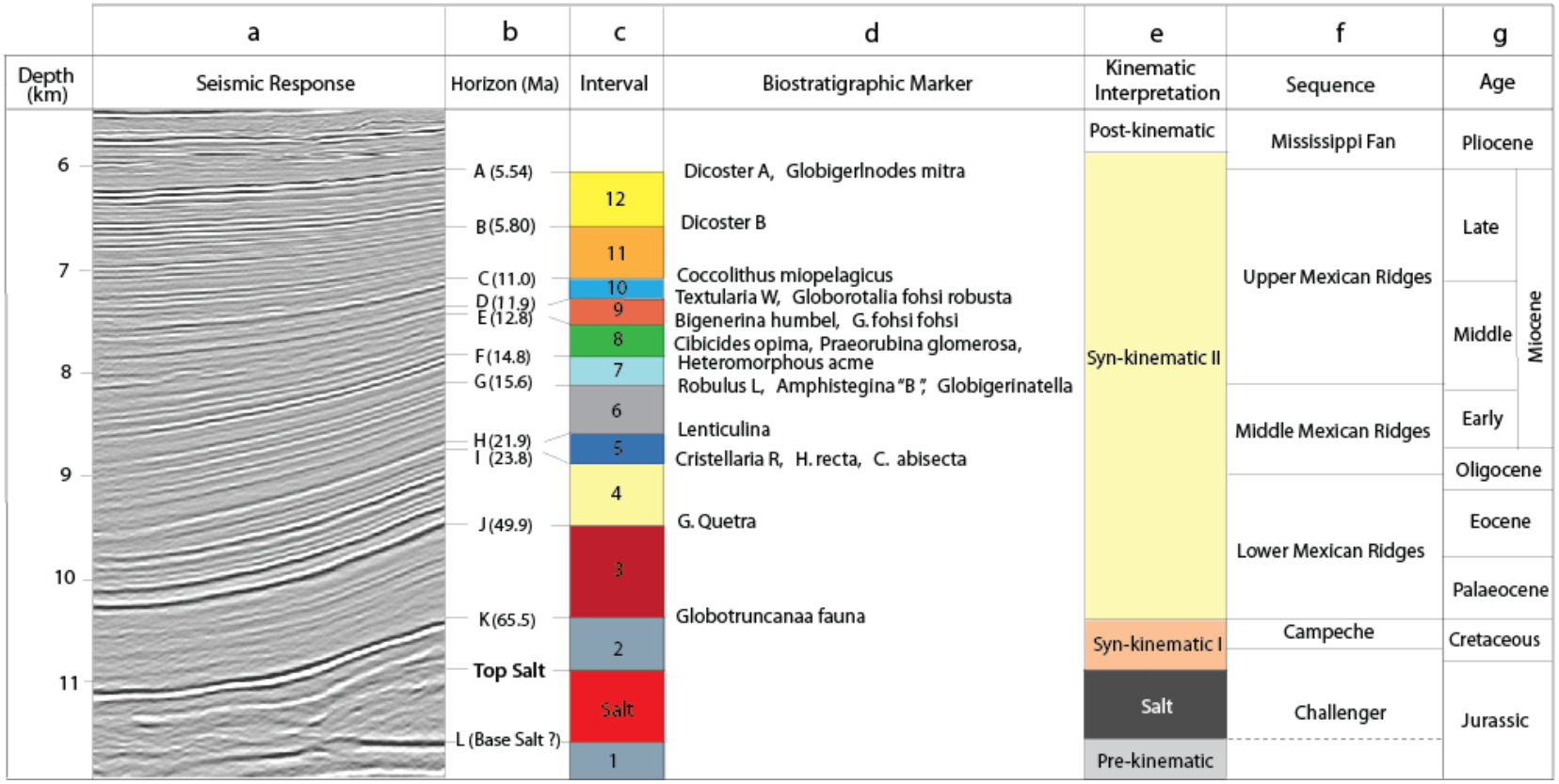

Figure 6. Seismic response (a), Interpreted seismic horizons and intervals (b,c), Biostratigraphic markers (d), Kinematic interpretation (e), Sequences (f) and Corresponding ages (g). Sequences in column f are defined by Weimer and Buffler, (1992).

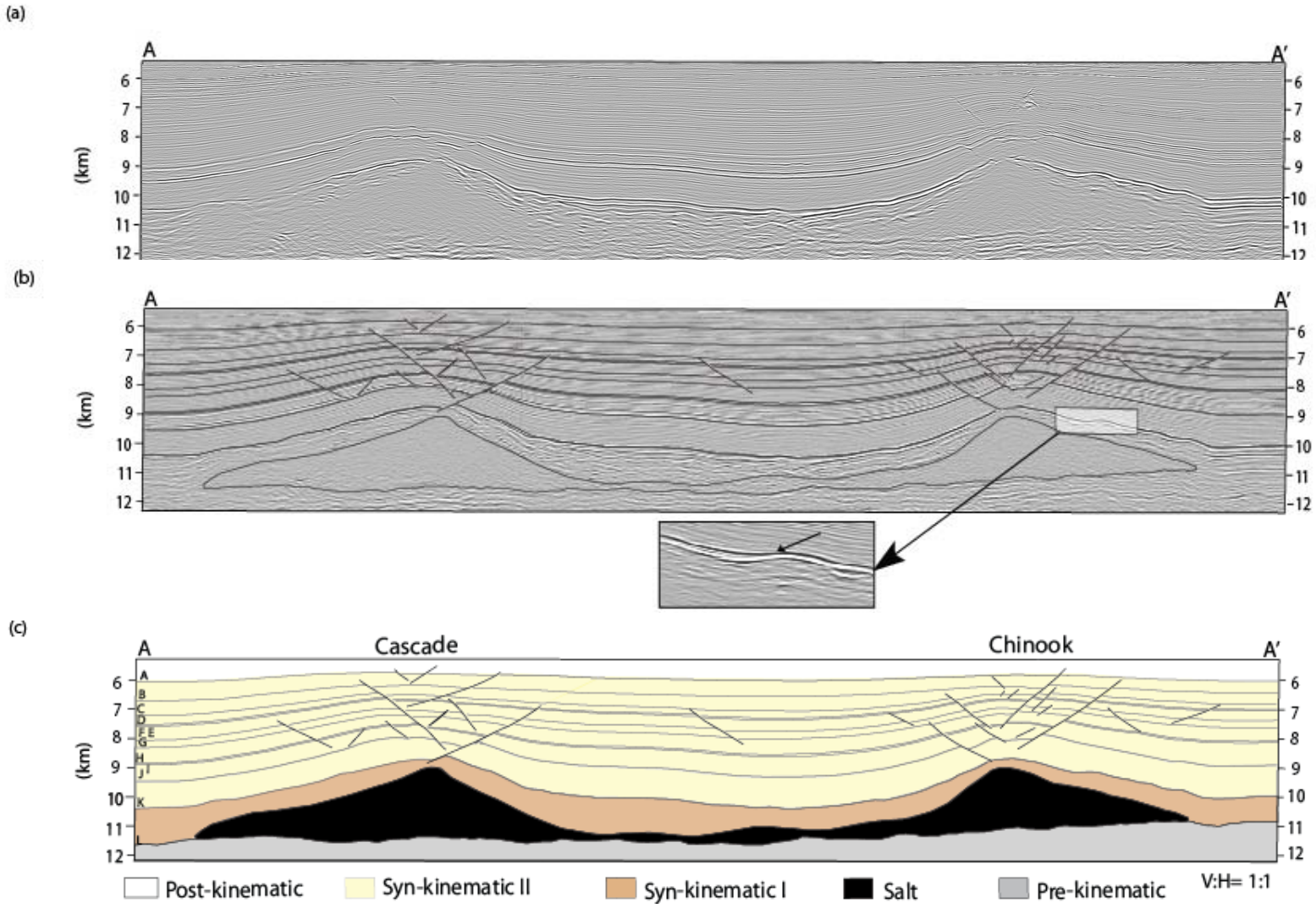

Figure 7. Profile A-A' through the Cascade and Chinook folds. (a) Uninterpreted, (b) Traced seismic section with insert showing strata truncation on horizon *K*, (c) Interpreted section. See Figure 5 for location.

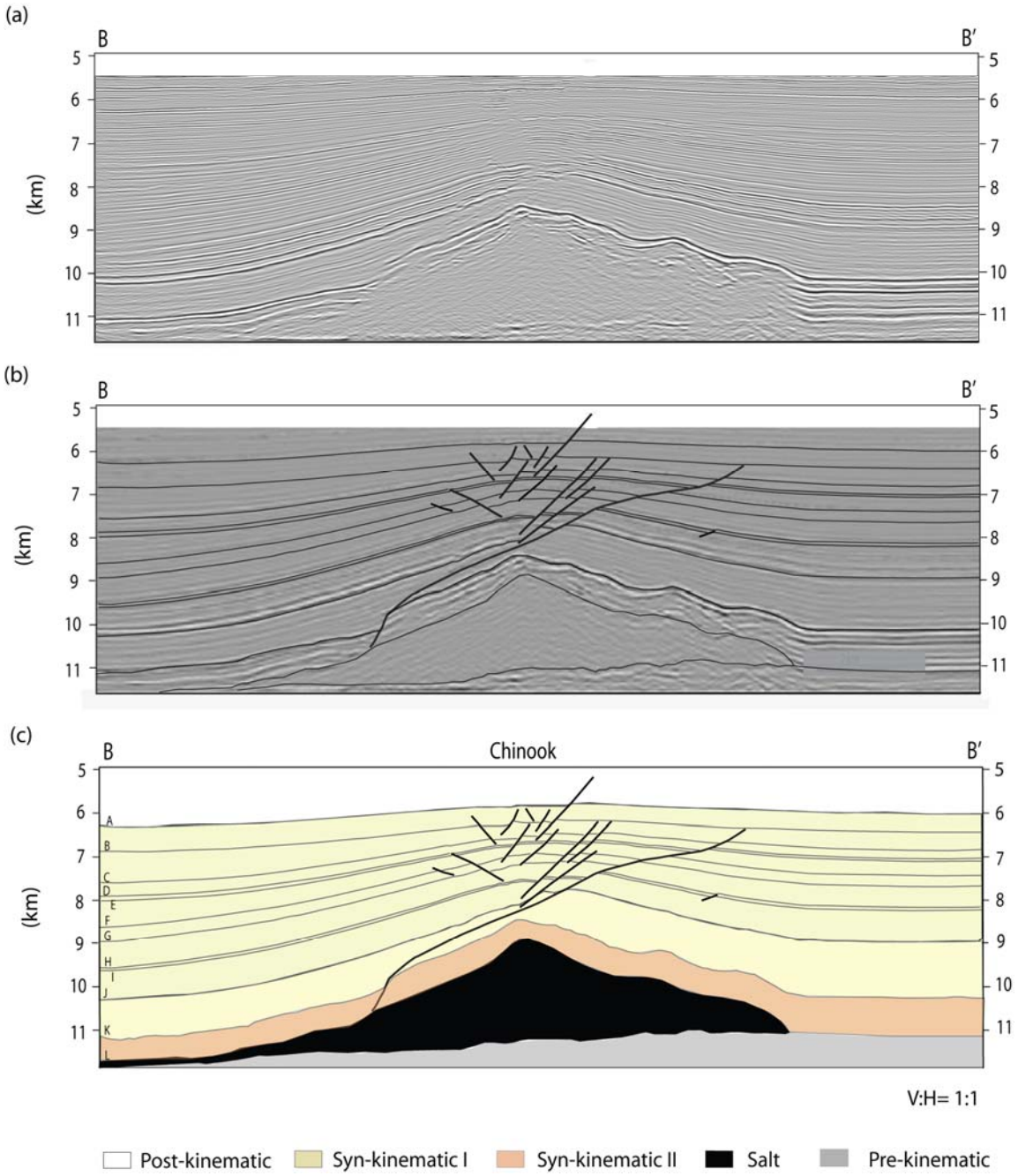

Figure 8. Profile B-B' through the Chinook fold. (a) Uninterpreted, (b) Traced seismic section and (c) Interpreted. See figure 5 for location.

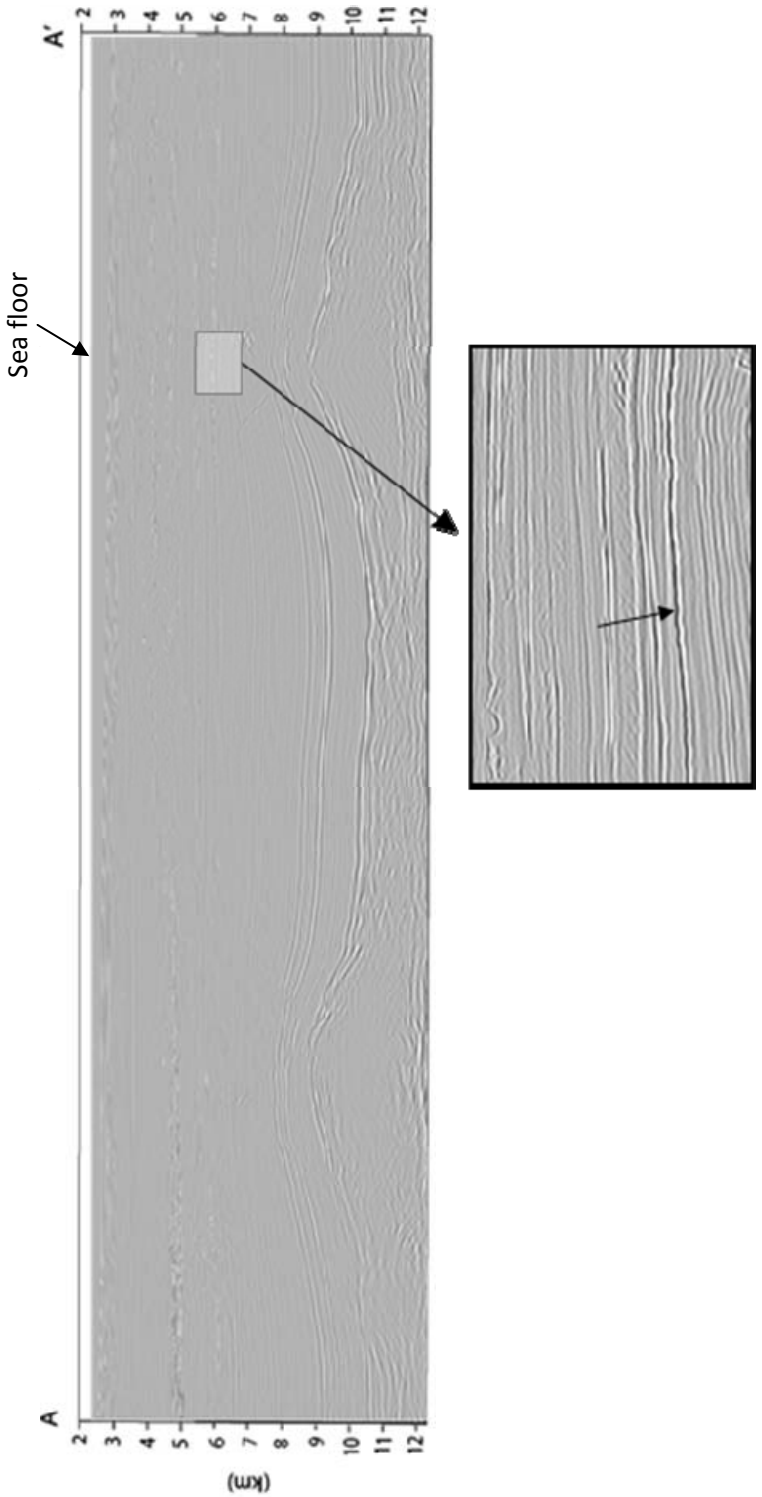

Figure 9 . Cascade and Chinook folds along section A-A'. The seafloor is approximately at 2.2 km below mean sea level. Insert showing onlap of post kinematic units onto interval 12.

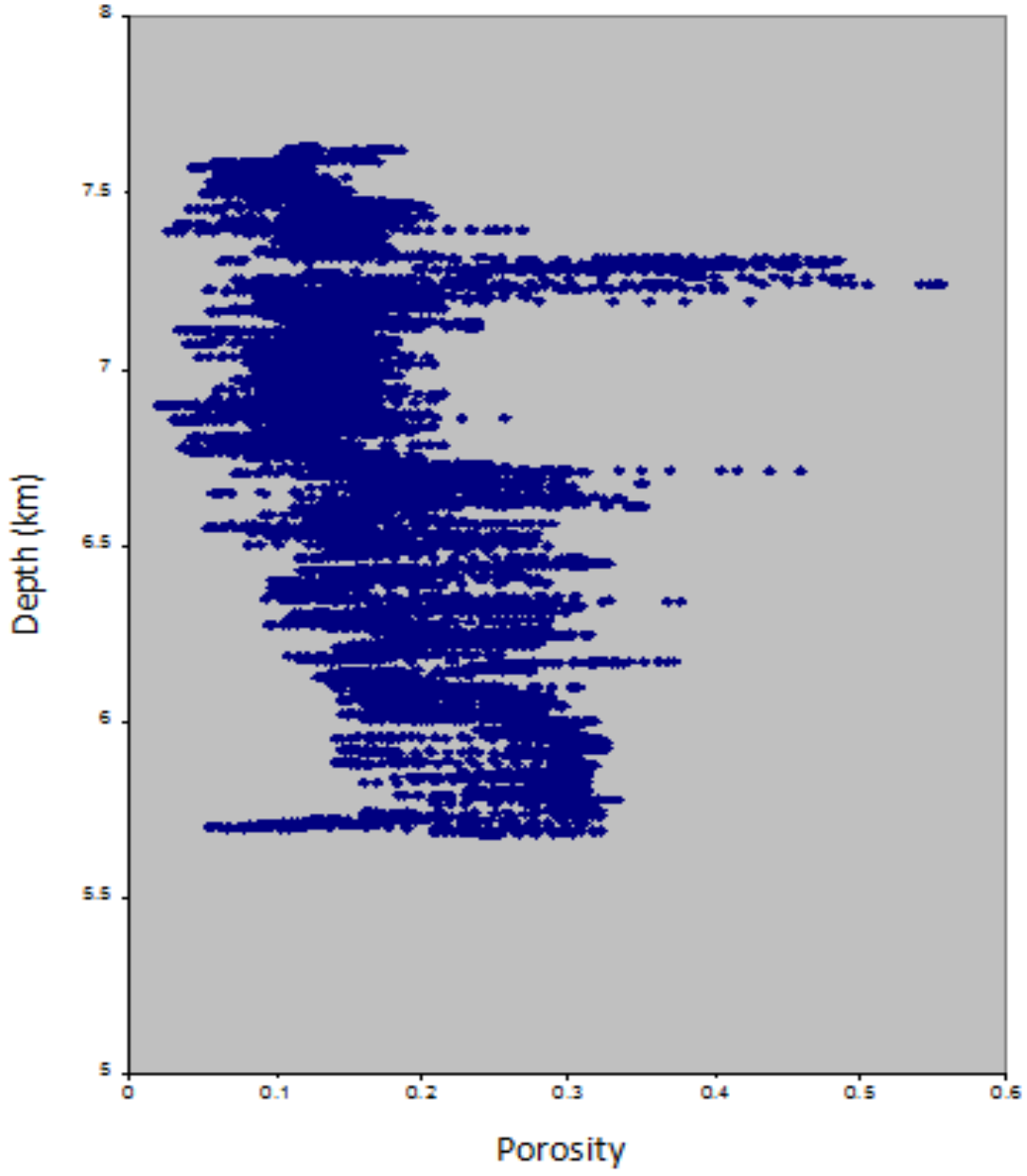

Figure 10. Plot of porosity values calculated from bulk density log data for every 0.15 m depth.

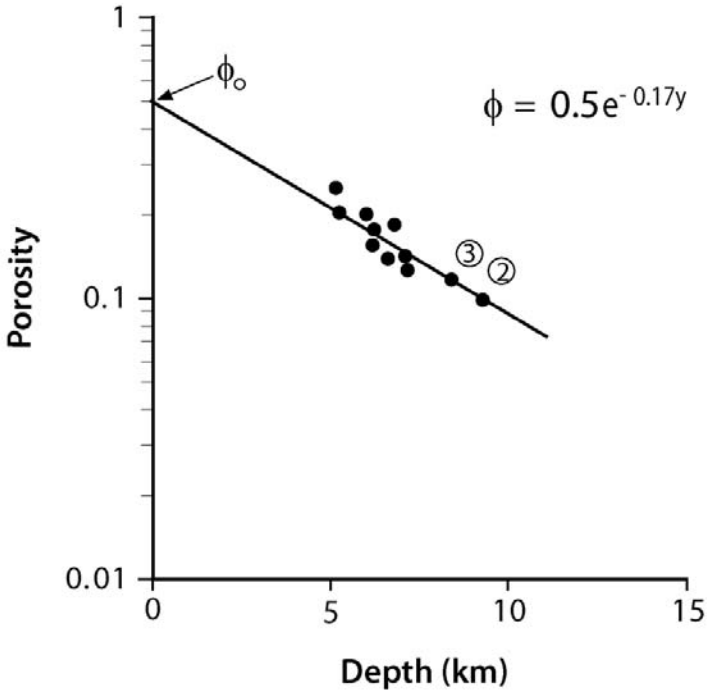

Figure 11. Porosity vs. depth plot extrapolated for intervals *2* and *3*.

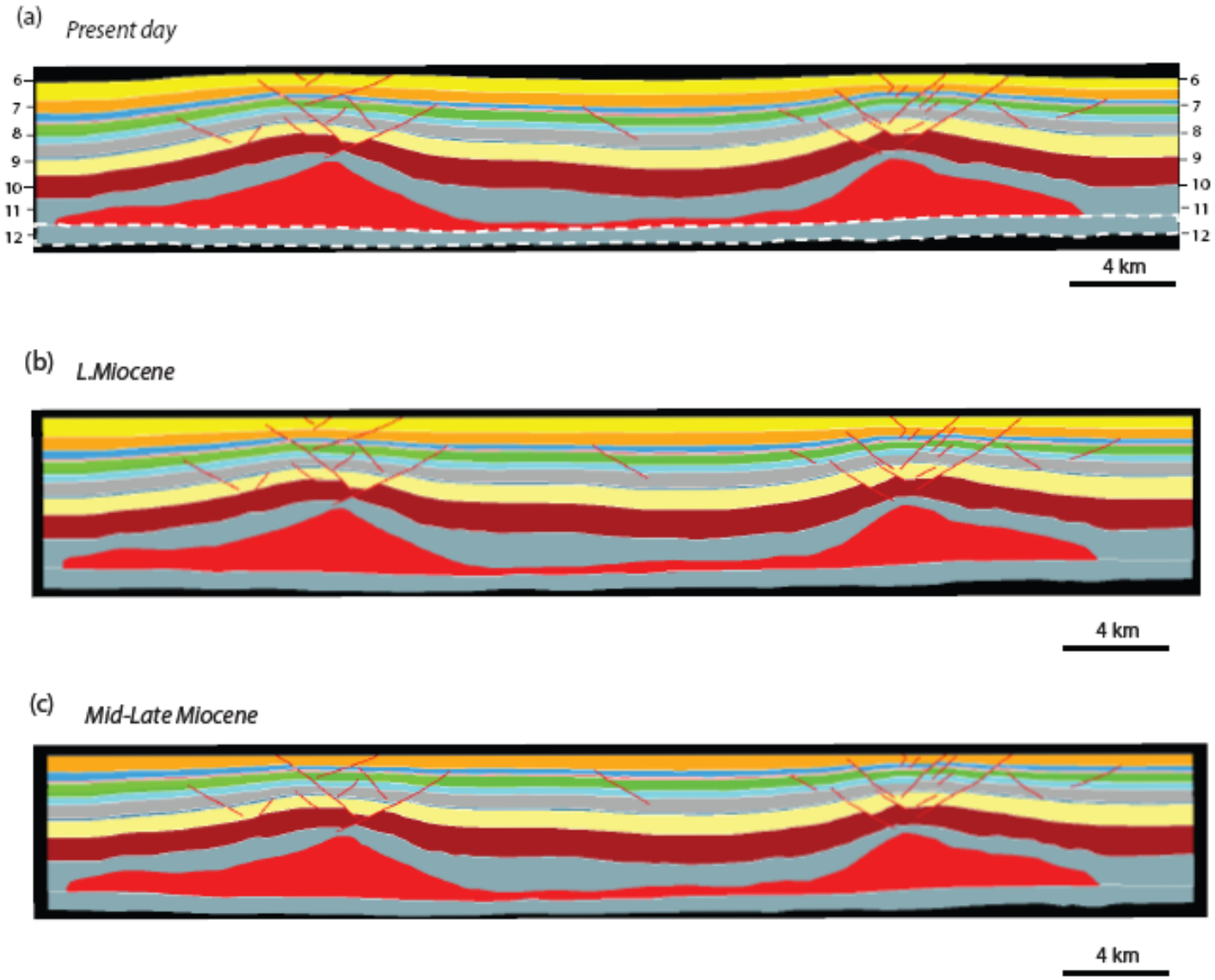

Figure 12. Sequential restorations of section A-A' through the Cascade and Chinook folds. Interval *1* (Dashed) is kept constant throughout restoration.

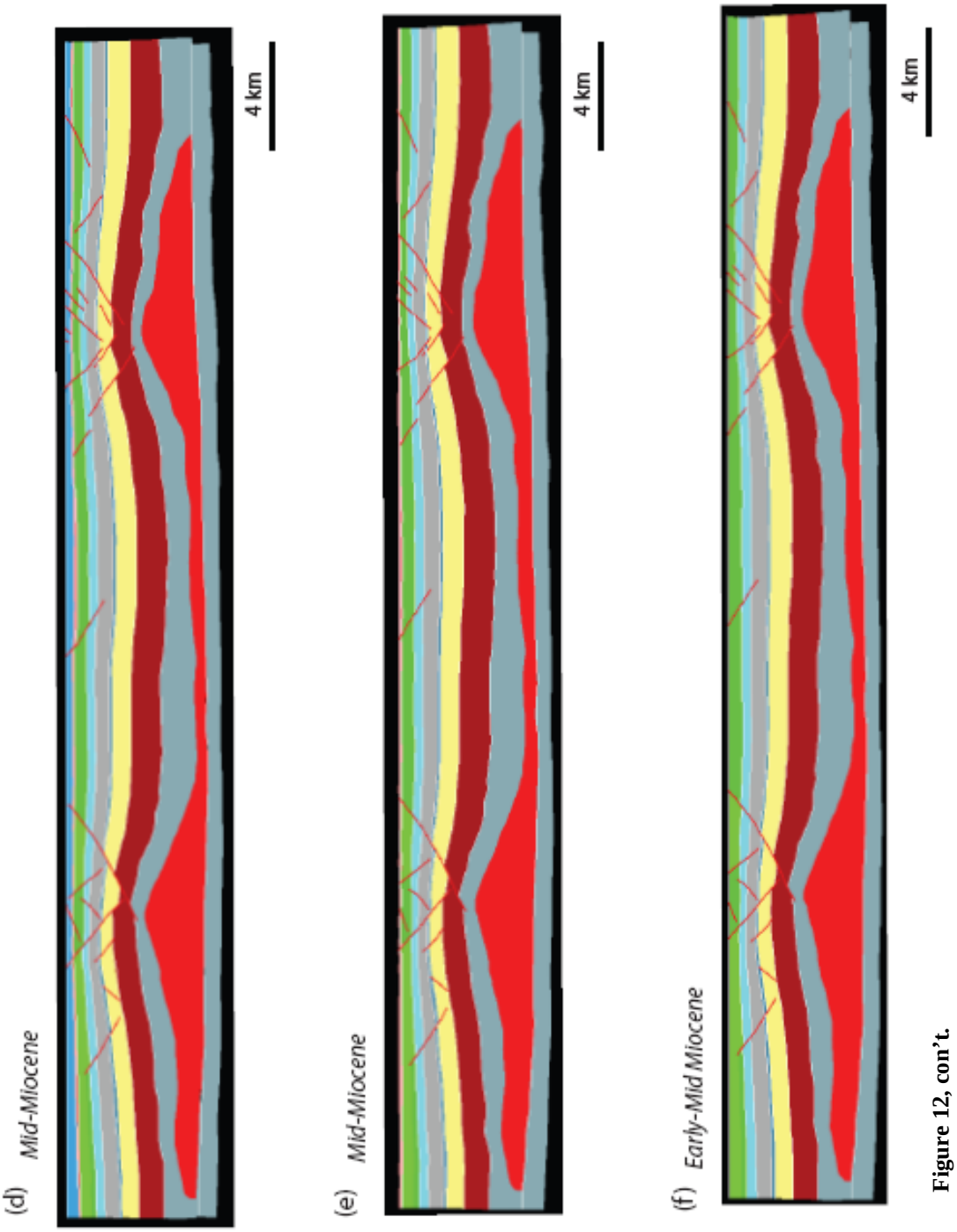

Figure 12, con't.

Figure 12, con't.

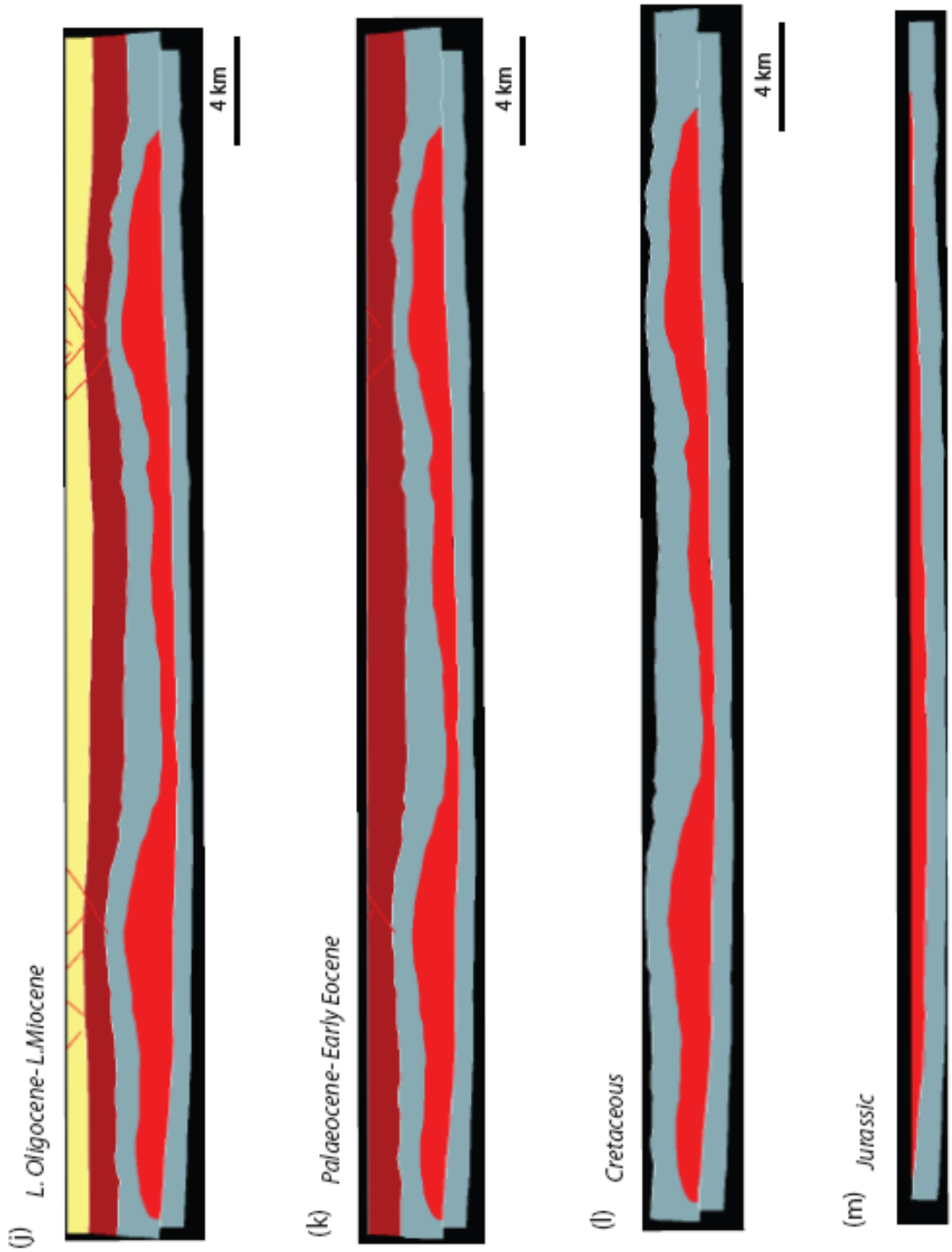

Figure 12, con't.

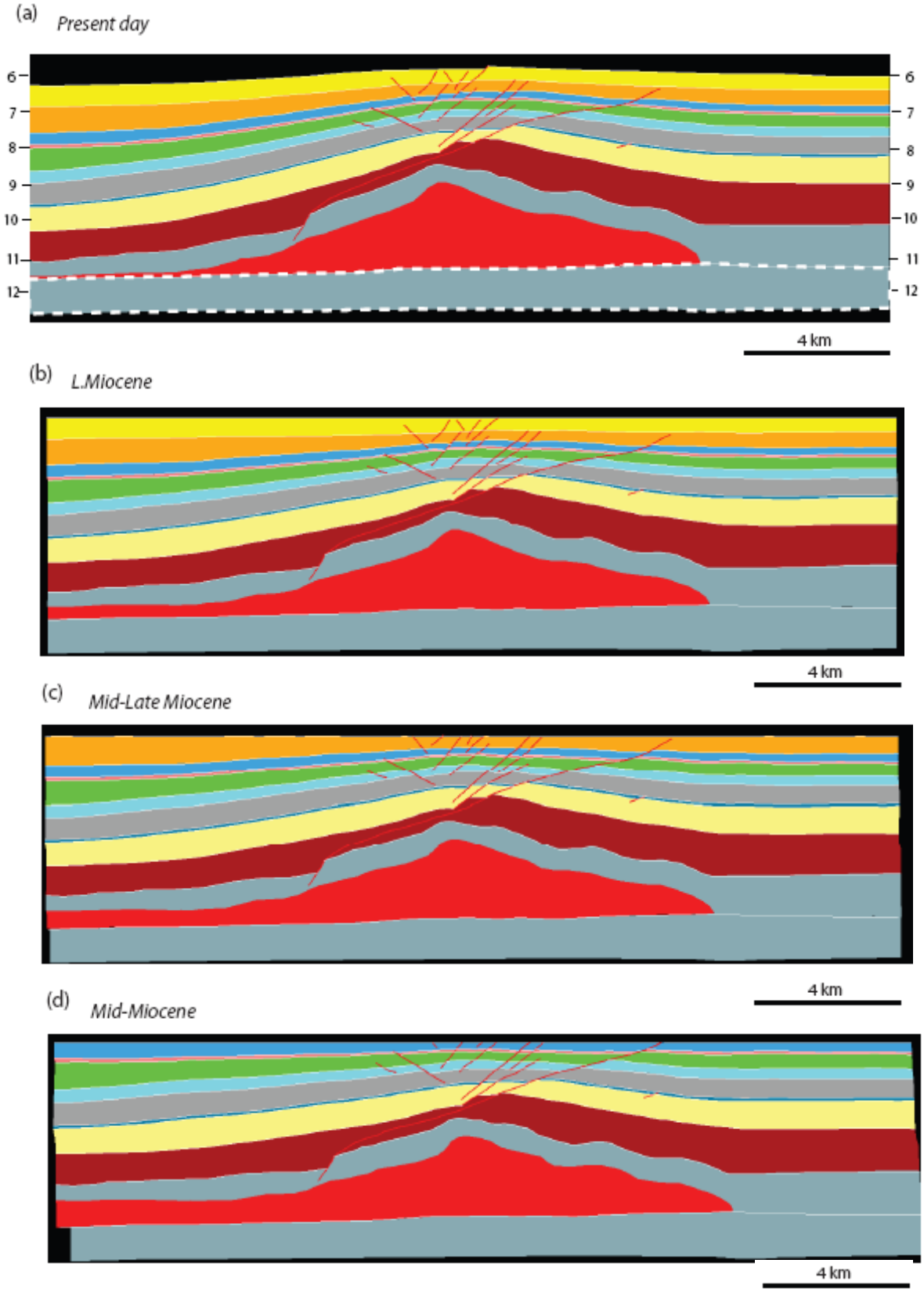

Figure 13. Sequential restorations of section B-B' through the Chinook fold. Interval *1* (Dashed) is kept constant throughout restoration.

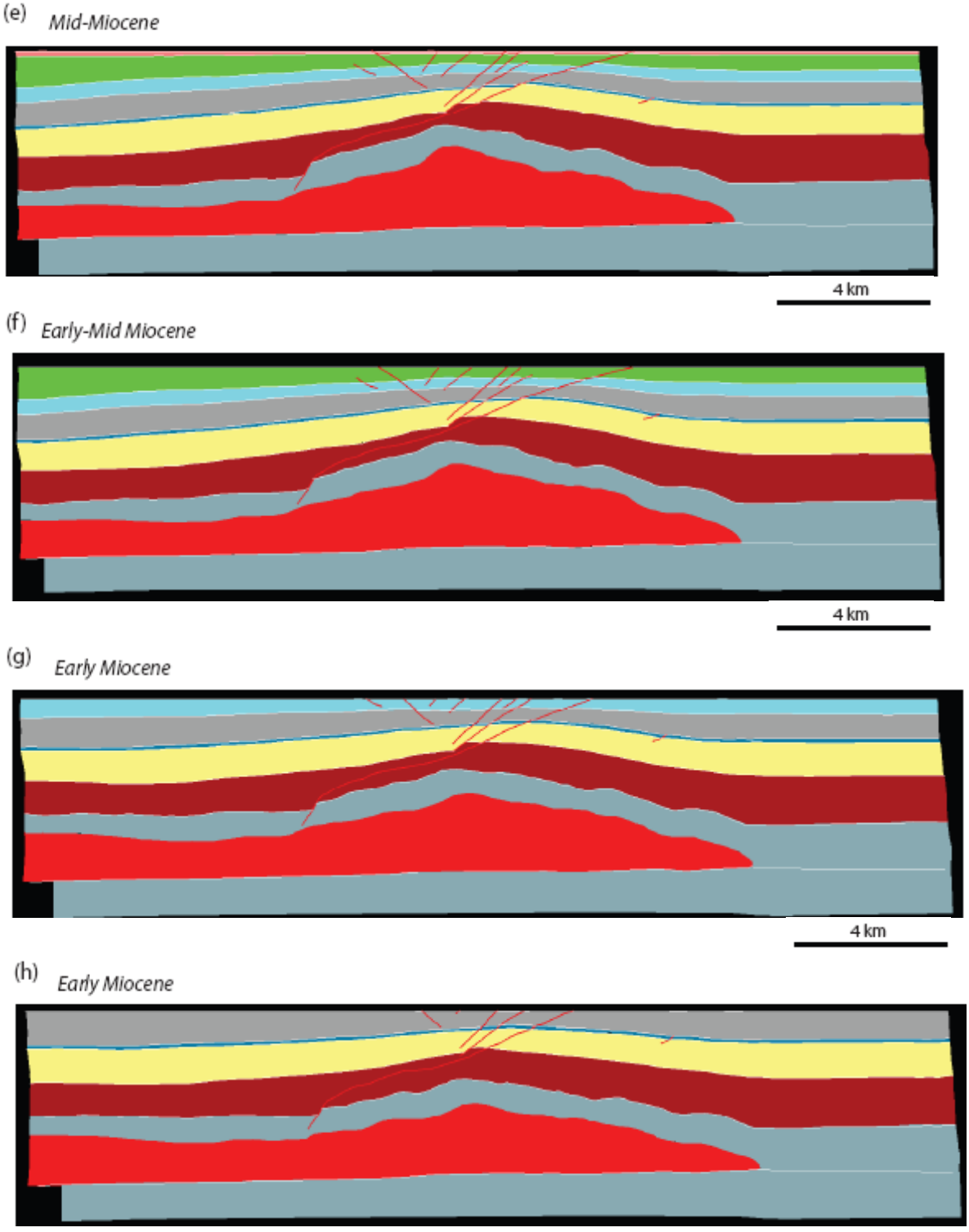

Figure 13, con't.

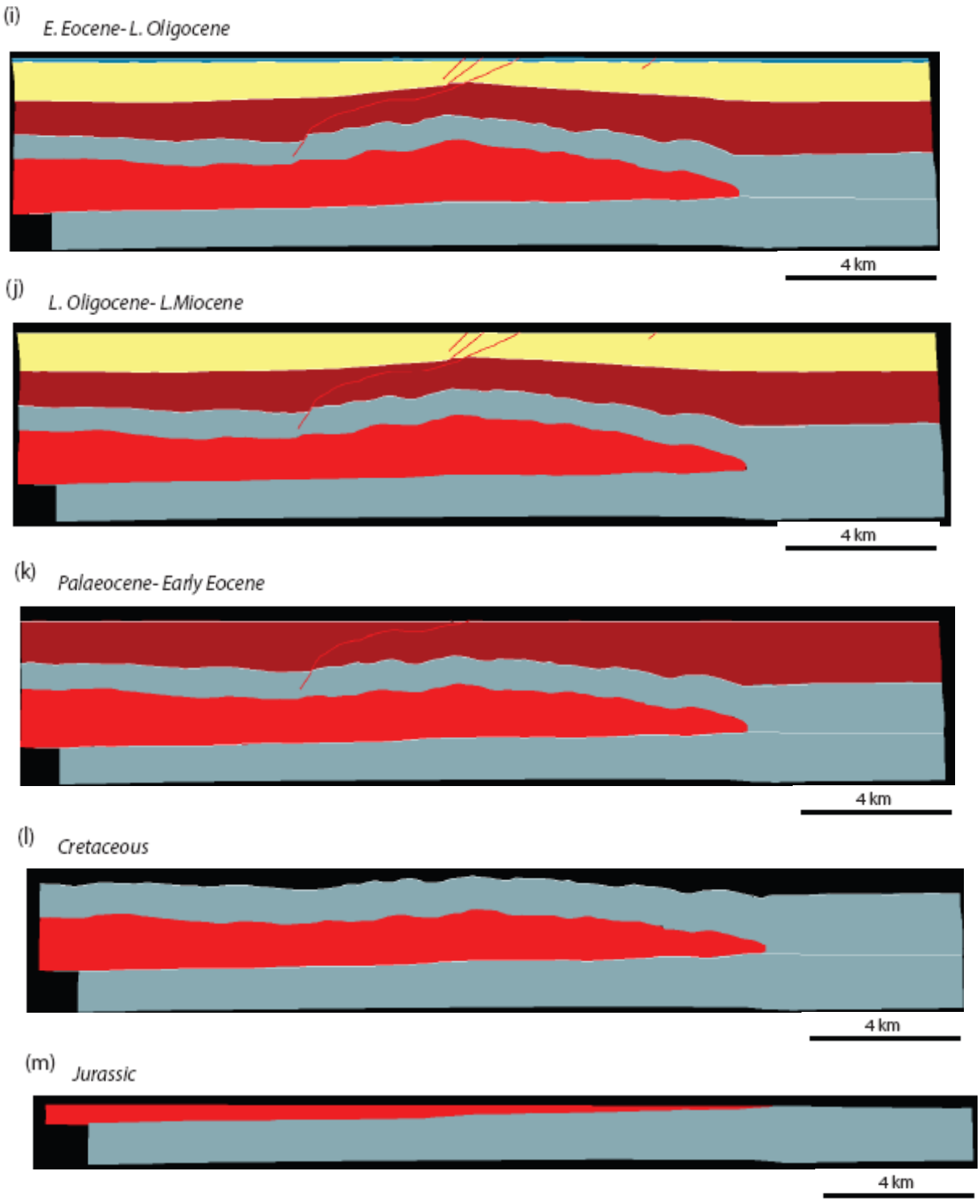

Figure 13, con't.

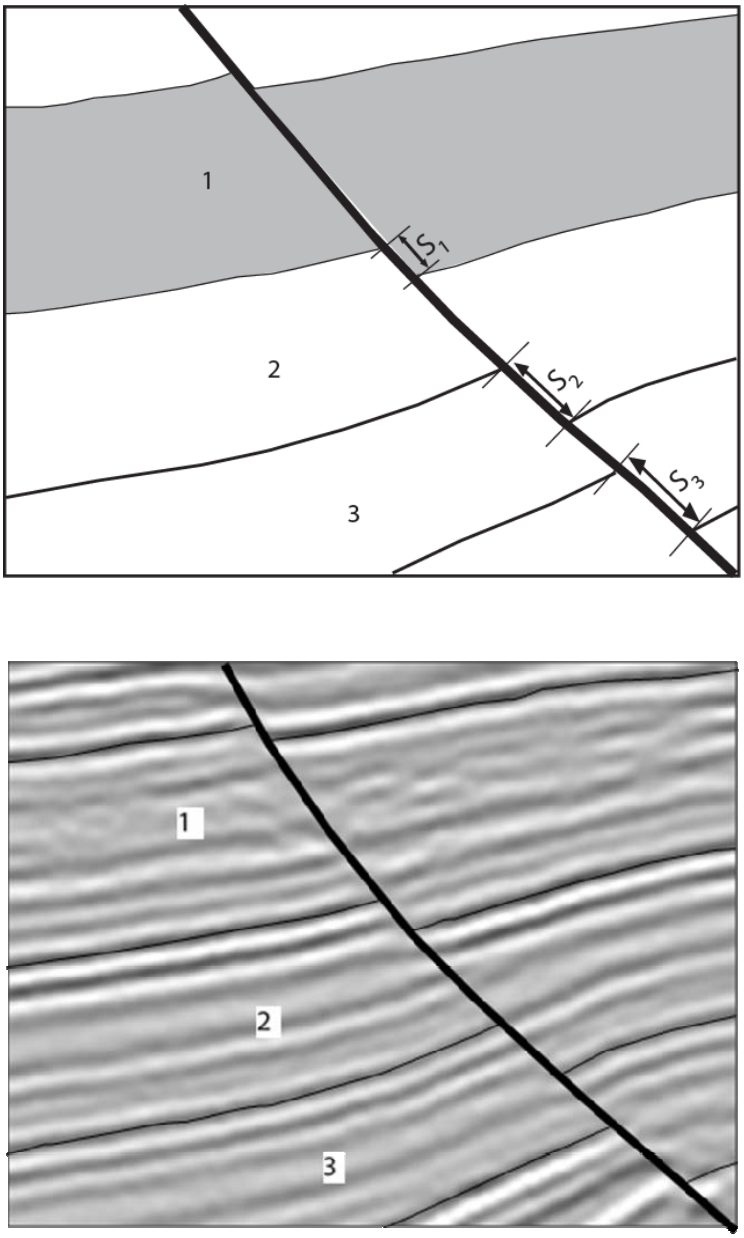

Figure 14. Method for measuring fault displacements (S_1, S_2 and S_3) across respective intervals (1, 2 and 3).

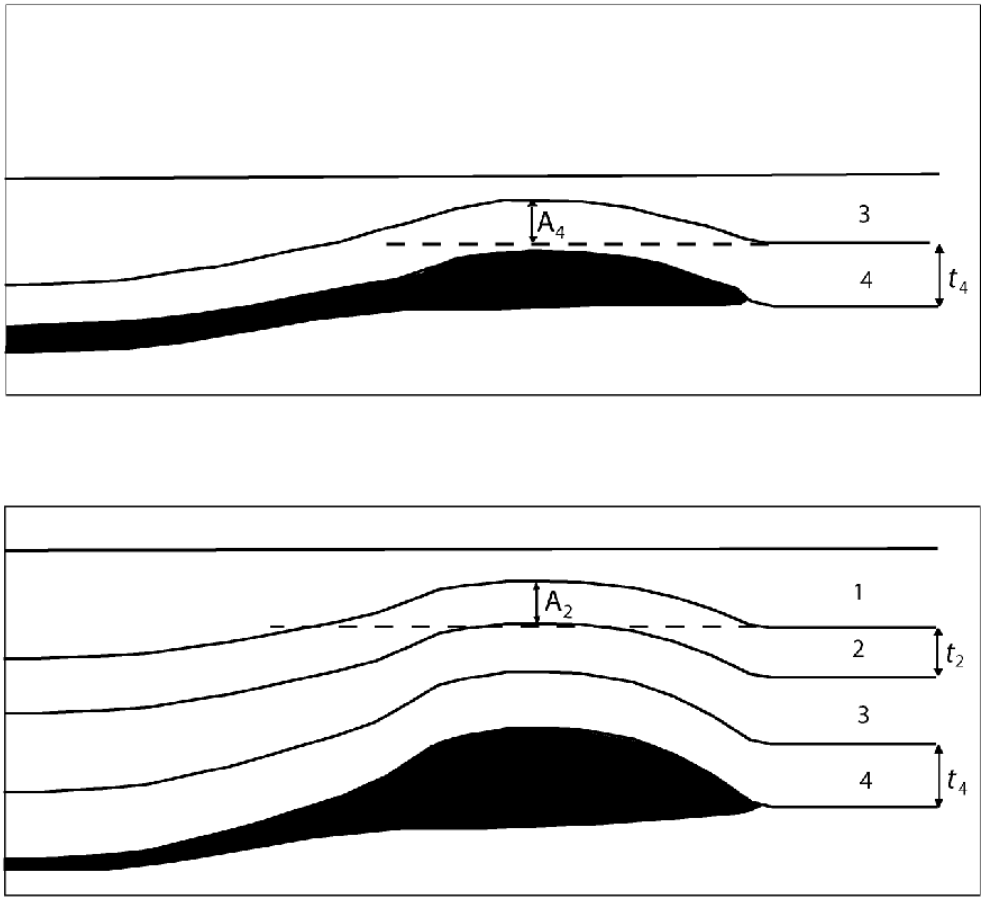

Figure 15. Method for measuring amplification (A_2 and A_4) of intervals during fold growth. Dividing by the corresponding time period (t_2, t_4) yields the fold growth rates for the Cascade and Chinook folds. (See table 2).

Figure 16. Method for measuring limb dips (θ_H, θ_I, θ_J), divided by periods of intervening intervals (t_3 and t_4) in deriving limb tilt rates for the Cascade and Chinook folds. See table 6.

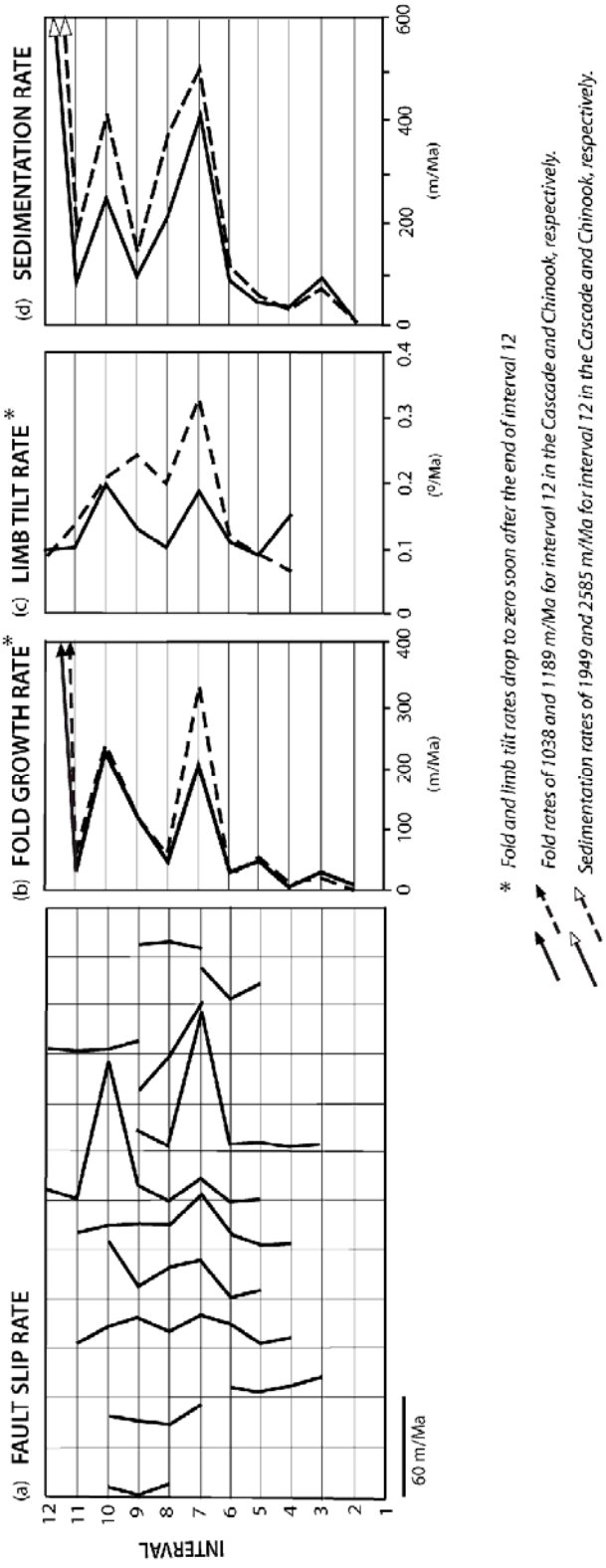

Figure 17. Cascade and Chinook rates of (a) slip for selected faults, (b) fold growth, (c) limb tilt and (d) sedimentation.

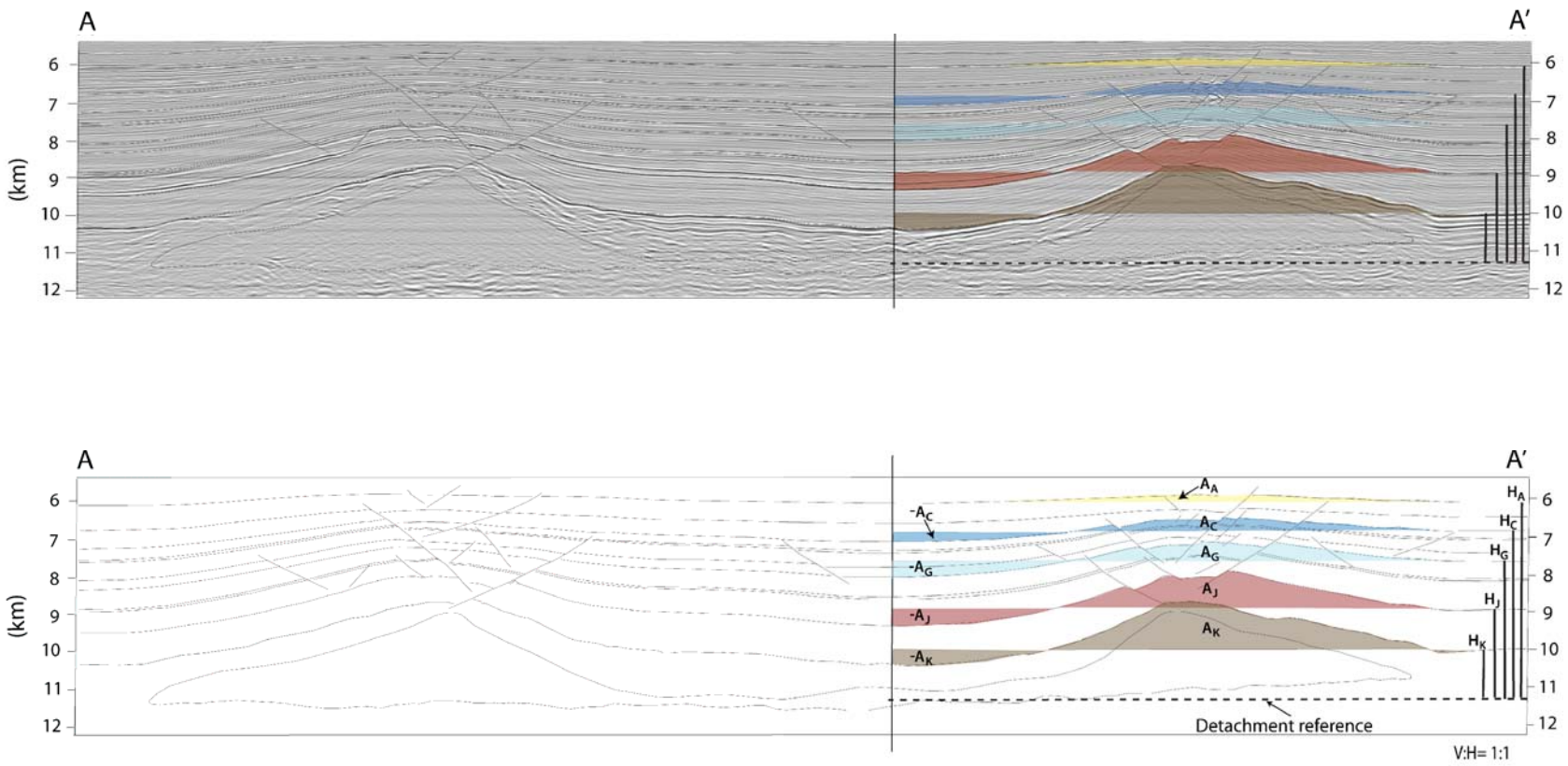

Figure 18. Fold area and depth to detachment measured for section A-A'. A_A, $-A_A$ and H_A are the anticlinal fold area, synclinal fold area and depth to detachment measured for horizon A, respectively. Polygons displayed are fold area measurements for horizons *A*, *C*, *G*, *J* and *K*.

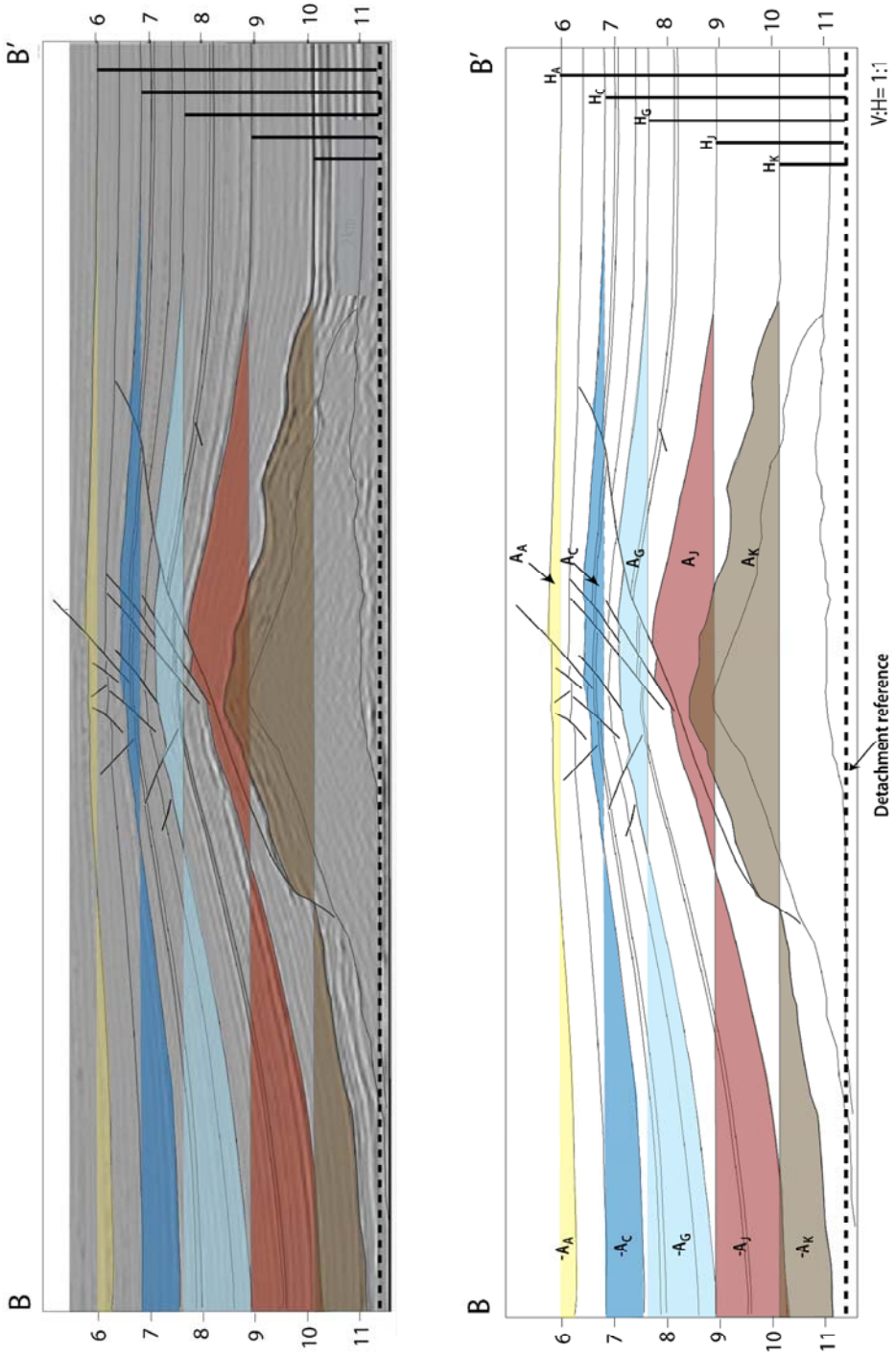

Figure 19. Fold area and depth to detachment measured for section B-B'. A_A, $-A_A$ and H_A are the anticlinal fold area, synclinal fold area and depth to detachment measured for horizon A, respectively. Polygons displayed are fold area measurements for horizons *A*, *C*, *G*, *J* and *K*.

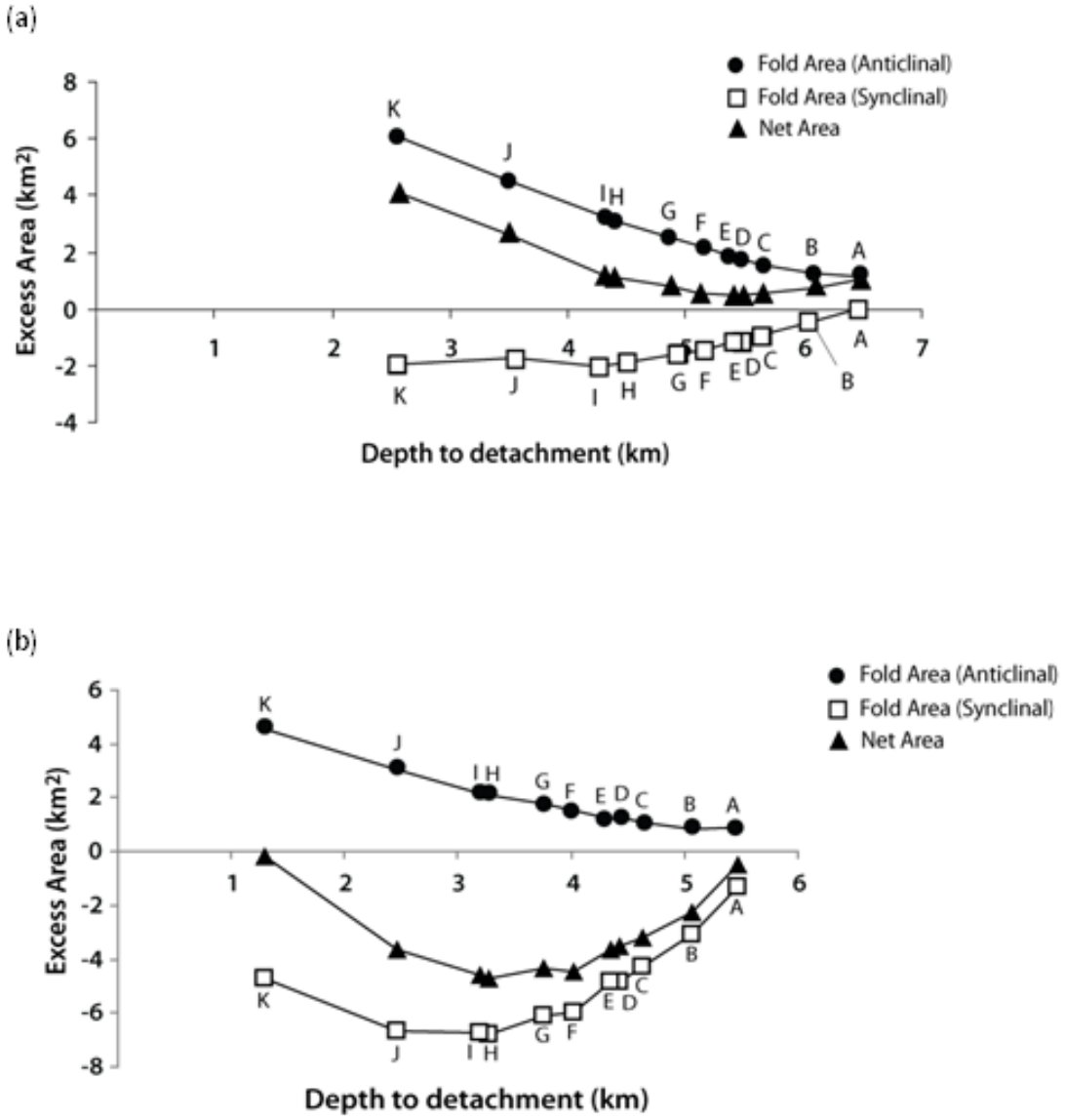

Figure 20. Fold area and depth to detachment plot for (a) section A'A', (b) section B-B'.

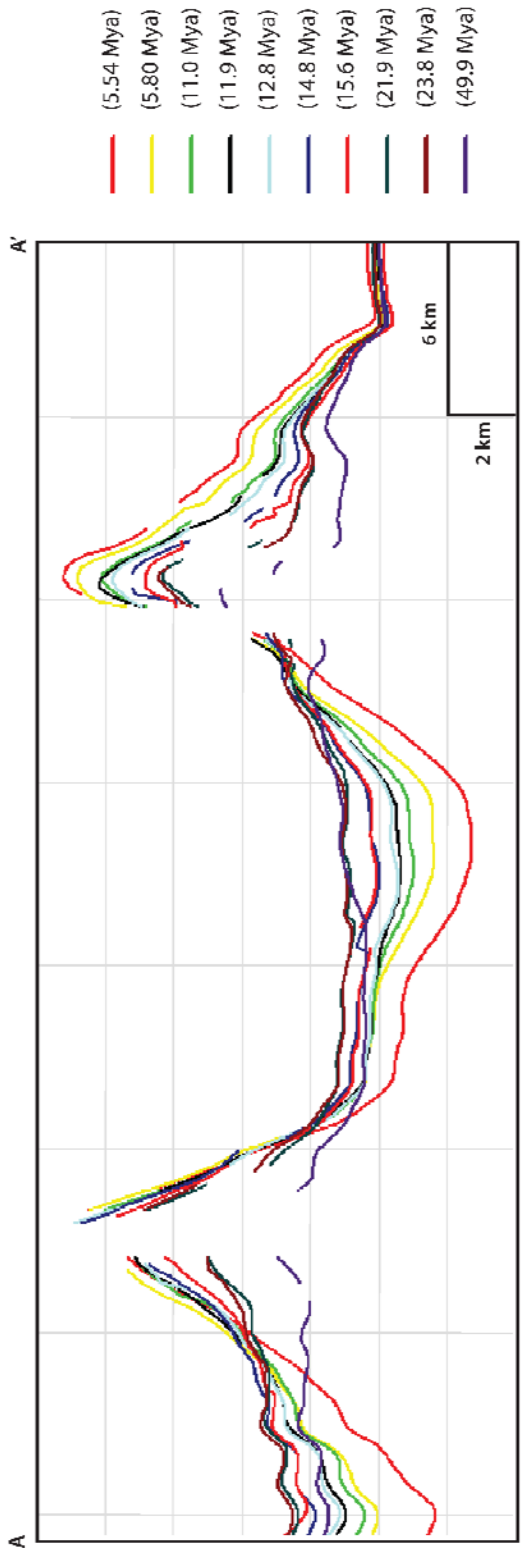

Figure 21. Evolution of horizon *K* through time across A-A'.

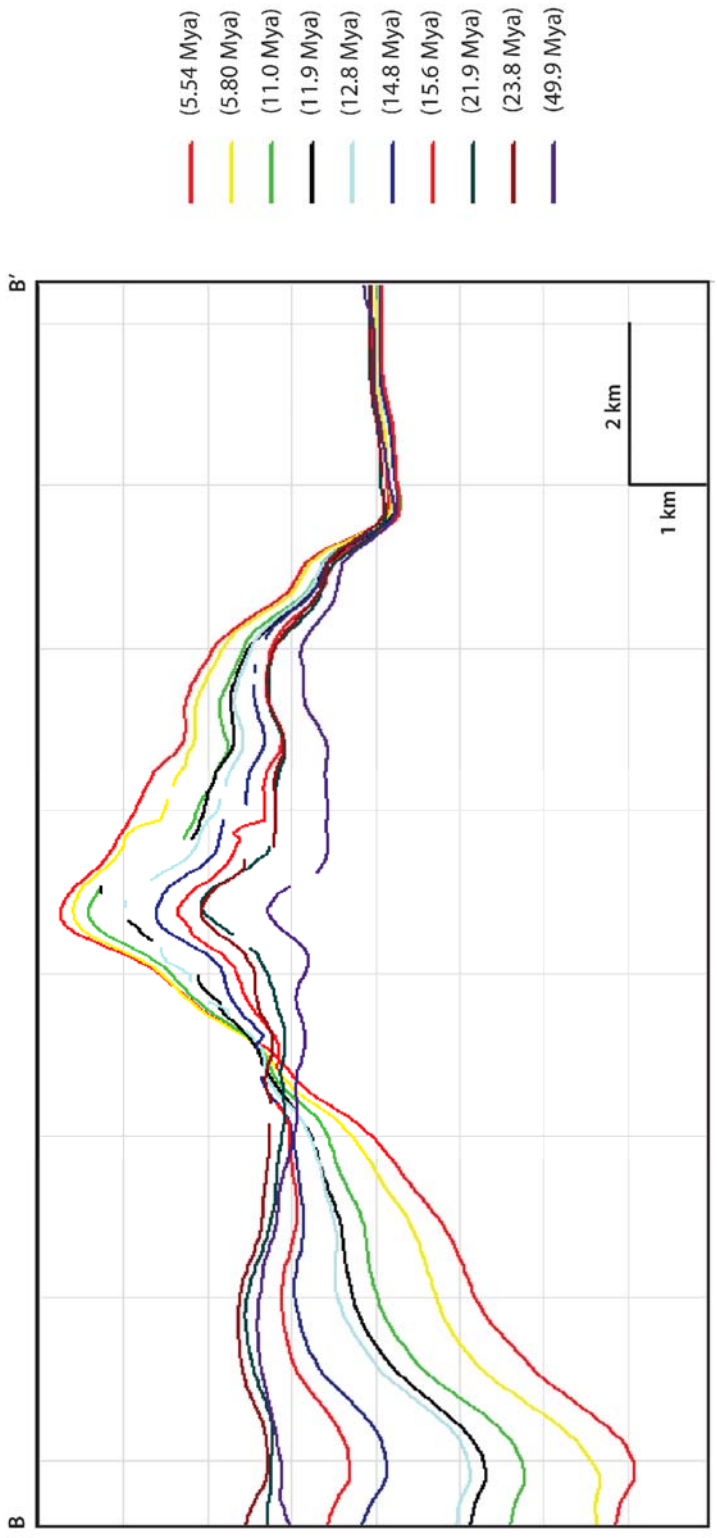

Figure 22. Evolution of horizon *K* through time across B-B'.

VITA

Name: Oluwatosin Eniola Majekodunmi

Address: Department of Geology and Geophysics, Texas A&M University, College Station, TX 77843-3115.

Email Address: tmajec@yahoo.com

Education: B.S., Geology, Florida International University, Miami, 2006.
M.S., Geology, Texas A&M University, College Station, 2009.